The SAURON project - XII. Kinematic substructures in early-type galaxies: evidence for disks in fast rotators

Davor Krajnović,[1][*] R. Bacon,[2] Michele Cappellari,[1] Roger L. Davies,[1]
P. T. de Zeeuw,[3,9] Eric Emsellem,[2] Jesús Falcón-Barroso,[4]
Harald Kuntschner,[5] Richard M. McDermid,[6] Reynier F. Peletier,[7]
Marc Sarzi,[8] Remco C. E. van den Bosch[9] and Glenn van de Ven[10][†]

[1] *Denys Wilkinson Building, University of Oxford, Keble Road, OX1 3RH, UK*
[2] *Université de Lyon, France; Université Lyon 1, F-69007; CRAL, Observatoire de Lyon, F-69230 Saint Genis Laval; CNRS, UMR 5574 ; ENS de Lyon, France*
[3] *European Southern Observatory, Karl-Schwarzschild-Str 2, 85748 Garching, Germany*
[4] *European Space and Technology Centre (ESTEC), Keplerlaan 1, Postbus 299, 2200 AG Noordwijk, The Netherlands*
[5] *Space Telescope European Coordinating Facility, European Southern Observatory, Karl-Schwarzschild-Str 2, 85748 Garching, Germany*
[6] *Gemini Observatory, Northern Operations Center, 670 N. A'ohoku Place,Hilo, Hawaii, 96720, USA*
[7] *Kapteyn Astronomical Institute, Postbus 800, 9700 AV Groningen, The Netherlands*
[8] *Centre for Astrophysics Research, University of Hertfordshire, Hatfield, Herts AL1 09AB*
[9] *Sterrewacht Leiden, Leiden University, Niels Bohrweg 2, 2333 CA Leiden, The Netherlands*
[10] *Institute for Advanced Study, Peyton Hall, Princeton, NJ 08544, USA*

9 July 2008

ABSTRACT

We analysed two-dimensional maps of 48 early-type galaxies obtained with the SAURON and OASIS integral-field spectrographs using kinemetry, a generalisation of surface photometry to the higher order moments of the line-of-sight velocity distribution (LOSVD). The maps analysed include: reconstructed image, mean velocity, velocity dispersion, h_3 and h_4 Gauss-Hermite moments. Kinemetry is a good method to recognise structures otherwise missed by using surface photometry, such as embedded disks and kinematic sub-components. In the SAURON sample, we find that 31% of early-type galaxies are single component systems. 91% of the multi-components systems have two kinematic subcomponents, the rest having three. In addition, 29% of galaxies have kinematically decoupled components, nuclear components with significant kinematic twists. We differentiate between slow and fast rotators using velocity maps only and find that fast rotating galaxies contain disks with a large range in mass fractions to the main body. Specifically, we find that the velocity maps of fast rotators closely resemble those of inclined disks, except in the transition regions between kinematic subcomponents. This deviation is measured with the kinemetric k_5/k_1 ratio, which is large and noisy in slow rotators and about 2% in fast rotators. In terms of E/S0 classification, this means that 74% of Es and 92% of S0s have components with disk-like kinematics. We suggest that differences in k_5/k_1 values for the fast and slow rotators arise from their different intrinsic structure which is reflected on the velocity maps. For the majority of fast rotators, the kinematic axial ratios are equal to or less than their photometric axial ratios, contrary to what is predicted with isotropic Jeans models viewed at different inclinations. The position angles of fast rotators are constant, while they vary abruptly in slow rotators. Velocity dispersion maps of face-on galaxies have shapes similar to the distribution of light. Velocity dispersion maps of the edge-on fast rotators and all slow rotators show differences which can only be partially explained with isotropic models and, in the case of fast rotators, often require additional cold components. We constructed local (bin-by-bin) $h_3 - V/\sigma$ and $h_4 - V/\sigma$ diagrams from SAURON observations. We confirm the classical anti-correlation of h_3 and V/σ, but we also find that h_3 is almost zero in some objects or even weakly correlated with V/σ. The distribution of h_4 for fast and slow rotators is mildly positive on average. In general, fast rotators contain flattened components characterised by a disk-like rotation. The difference between slow and fast rotators is traceable throughout all moments of the LOSVD, with evidence for different intrinsic shapes and orbital contents and, hence, likely different evolutionary paths.

Key words: galaxies: elliptical and lenticular - galaxies: kinematics and dynamics - galaxies: structure - galaxies:evolution

1 INTRODUCTION

The classification of galaxies both acknowledges the complexity of these celestial objects and attempts to understand their formation and evolution. The Hubble Classification of galaxies (Hubble 1936; Sandage 1961; Sandage et al. 1975; Sandage & Bedke 1994) recognises the dichotomy between, broadly speaking, disk and elliptical galaxies, for historical reasons now often called late- and early-types. The classification works well on the late-type galaxies in particular, dividing the class into a number of subgroups which correlate with properties such as bulge-to-disk ratio, morphology of spiral arms, gas and dust content, to name a few, but it fails to bring a physical insight to our understanding of early-types (Tremaine 1987), where the classification is based on apparent shape and thus dependant on viewing angles.

In an effort to eliminate the unsatisfactory situation Kormendy & Bender (1996) proposed a revision of the Hubble classification. It was based on two discoveries in the 1970s and 1980s, both enabled by an improvement in the technical capabilities of astronomical instruments. A series of papers (Bertola & Capaccioli 1975; Illingworth 1977) showed that bright elliptical galaxies do not rotate as fast as they should, if they were oblate isotropic systems supported by rotation (Binney 1978), whereas less bright and generally smaller systems, including also bulges of spirals, generally agree with such predictions (Davies et al. 1983; Kormendy 1982; Kormendy & Illingworth 1982). A complementary discovery (Bender 1988b; Bender et al. 1988, 1989) that the fast rotating galaxies are more likely to have disky isophotes, while the slow rotating galaxies have boxy isophotes, linked again the kinematics and shape of galaxies. Kormendy & Bender (1996) changed the uniformity of early-type galaxies to a dichotomy (disky vs boxy, fast vs slow, brighter vs less bright) and linked the whole Hubble sequence from right to left, from Sc–Sb–Sa to S0–E types, where 'rotation decreases in dynamical importance compared to random motions'.

This important step forward introduced a readily measurable parameter related to some physical properties. However, the higher order variations in the isophotal shape (diskiness/boxiness) are not measurable at all inclinations regardless of the prominence of the disks (Rix & White 1990), and finally, they are used to infer the dynamical state of the galaxy. This might be a decent approximation, especially if one assumes that all fast rotating galaxies comprise of spheroidal slow rotating components and disks seen at different inclination (Rix et al. 1999), but the edge-on observations of spheroidal components in spiral galaxies showed that bulges are rotating fast as well (Kormendy & Illingworth 1982). To complicate things further the updated classification continues to distinguish S0s from Es, keeping a viewing angle dependent definition of S0s (van den Bergh 1990).

The choice of using the fourth order Fourier term in the isophotometric analysis for classification is natural, because *(i)* it is much easier to take images of galaxies than to measure their kinematics, and *(ii)* until recently it was not realistic to spectroscopically map their two-dimensional structure. The advent of panoramic integral-field units, such as SAURON (Bacon et al. 2001), is changing the technical possibilities and the field itself; it is now possible to systematically map kinematics of nearby galaxies up to their effective radii. We have observed 72 nearby E, S0 and Sa galaxies as part of the SAURON survey (de Zeeuw et al. 2002, hereafter Paper II). Focusing here on a subsample of 48 early-type galaxies (E, S0), these observations clearly show the previously hinted rich variety of kinematic substructures such as: kinematically decoupled

cores, kinematic twists, counter-rotating structures and central disks (Emsellem et al. 2004, hereafter Paper III).

Analysing the global properties of the SAURON velocity and velocity dispersion maps, Emsellem et al. (2007, hereafter Paper IX) were able to separate the early-type galaxies into two physically distinct classes of *slow* and *fast* rotators, according to their specific (projected) angular momentum measured within one effective radius, λ_R. This finding augments the view that led to the revision of the classification, but the SAURON observations provide the crucial quantitive data. Moreover, the results of Paper IX suggest a way to dramatically improve on the Hubble classification and substitute S0s and (misclassified) disky ellipticals with one class of fast rotators.

Cappellari et al. (2007, hereafter Paper X) addressed again the issue of orbital anisotropy of early-type galaxies. They constructed the $(V/\sigma, \epsilon)$ diagram (Binney 1978) using an updated formalism (Binney 2005), and compared it with the results from general axisymmetric dynamical models for a subsample of these galaxies (Cappellari et al. 2006, hereafter Paper IV). They found that slow and fast rotators are clearly separated on the $(V/\sigma, \epsilon)$ diagram (unlike Es and S0s), such that slow rotators are round, moderately isotropic and are likely to be somewhat triaxial, while fast rotators appear flattened, span a larger range of anisotropies, but are mostly oblate axisymmetric objects. This finding is in a partial agreement with previous studies which either found round early-type galaxies radially anisotropic (van der Marel 1991), moderately radially anisotropic (Gerhard et al. 2001) or only weakly anisotropic with a range of anisotropies for flattened systems (Gebhardt et al. 2003). The results of Paper X, however, clearly show that intrinsically flatter galaxies tend to be more anisotropic in the meridional plane. The models also indicate that the fast rotators are often two component systems, having also a flat and rotating, kinematically distinct, disk-like component.

Dynamical models are often time consuming and difficult to construct. Ultimately, one would like to be able to classify galaxies by their observable properties only. Is it possible to learn about the intrinsic shapes of the early-type galaxies from observations only? Surface photometry, being but the zeroth moment of the ultimate observable quantity for distant galaxies, the line-of-sight velocity distribution (LOSVD), cannot give the final answer. It is necessary to look at the other moments of the LOSVD: mean velocity, velocity dispersion and higher-order moments, commonly parameterised by Gauss–Hermite coefficients, h_3 and h_4 (van der Marel & Franx 1993; Gerhard 1993), which measure asymmetric and symmetric deviation of the LOSVD from a Gaussian, respectively.

Indeed, in the last dozen years several studies investigated higher moments of the LOSVD of early-type galaxies observing them along one or multiple slits (e.g. Bender et al. 1994; van der Marel et al. 1994; van der Marel 1994; Kronawitter et al. 2000; Koprolin & Zeilinger 2000; Halliday et al. 2001; Wegner et al. 2002; Hau & Forbes 2006; Corsini et al. 2008). These studies deepened the dichotomy among early-type galaxies showing that fast rotating galaxies with disky isophotes also exhibit an anti-correlation between h_3 and V/σ. This is consistent with these galaxies being made of two components: a bulge and a disk. The symmetric deviations, on the other hand are usually smaller than asymmetric ones, and somewhat positive in general. In addition, the observed higher order moments of the LOSVD can be used to constrain the possible merger scenarios of early-type galaxies and their formation in general (e.g. Balcells 1991; Bendo & Barnes 2000; González-García et al. 2006; Naab et al. 2006; Jesseit et al.

2007). However, observations along one or two slits are often not able to describe the kinematical richness of early-type galaxies.

In this work we use *kinemetry* (Krajnović et al. 2006), a generalisation of surface photometry to all moments of the LOSVD, to study SAURON maps of 48 early-type galaxies. The purpose of this work is to investigate observational clues from resolved two-dimensional kinematics for the origin of the differences between the slow and fast rotators.

In Section 2 we briefly remind the reader of the SAURON observations and data reduction. Section 3 describes the methods and definitions used in this work. The main results are presented in Section 4. In Section 5 we offer an interpretation of the results and we summarise the conclusions in Section 6. In Appendix A we discuss the influence of seeing on the two-dimensional kinematics and in Appendix B we present the radial profiles of the kinematric coefficients used in this study.

2 SAMPLE AND DATA

In this work we used the data from the SAURON sample which was designed to be *representative* of the galaxy populations in the plane of ellipticity, ϵ, versus absolute B band magnitude M_B. The sample and its selection details are presented in Paper II. In this study we focus on the 48 galaxies of the SAURON E+S0 sample.

SAURON is an integral-field spectrograph with a field-of-view (FoV) of about $33'' \times 41''$ and $0.''94 \times 0.''94$ square lenses, mounted at the William Herschel Telescope. Complementing the SAURON large scale FoV, we probed the nuclear regions of a number of galaxies with OASIS, then mounted at Canada-Hawaii-France Telescope, a high spatial resolution integral-field spectrograph, similarly to SAURON based on the TIGER concept (Bacon et al. 1995). The FoV of OASIS is only $10'' \times 8''$, but the spatial scale is $0.''27 \times 0.''27$, fully sampling the seeing-limited point spread function and providing on average a factor of 2 improvement in spatial resolution over SAURON. The spectral resolution of OASIS is, however, about 20% lower than that of SAURON, and only a subsample of the SAURON galaxies was observed.

In this paper we are investigating the stellar kinematics of early-type galaxies. Paper III and McDermid et al. (2006, hereafter Paper VIII) discuss the extraction of kinematics and construction of maps of the mean velocity V, the velocity dispersion σ, and the Gauss-Hermite moments h_3 and h_4 in great detail. All maps used in this work are Voronoi binned (Cappellari & Copin 2003) to the same signal-to-noise ratio. The SAURON kinematic data used here are of the same kinematic extraction as in Paper X with the latest improvement on the template mismatch effects in higher moments of the LOSVD. The SAURON mean velocity maps are repeated in this paper for the sake of clarity, but we encourage the reader to have copies of both Paper III and Paper VIII available for reference on other moments of the LOSVD.

3 METHOD AND DEFINITIONS

Maps of the moments of the LOSVD offer a wealth of information, but also suffer from complexity. It is difficult, if not impossible, to show error bars for each bin on the map, and the richness of the maps can lead to the useful information being lost in detail. As in the case of imaging, it is necessary to extract the useful information from the maps to profit from their two-dimensional coverage of the

objects. In this section we describe the method used to analyse the maps and discuss definitions utilised throughout the paper.

3.1 Kinemetry

Krajnović et al. (2006) presented kinemetry, as a quantitative approach to analysis of maps of kinematic moments. Kinemetry is a generalisation of surface photometry to the higher-order moments of the LOSVD. The moments of the LOSVD have odd or even parity. The surface brightness (zeroth moment) is even, the mean velocity (first moment) is odd, the velocity dispersion (second moment) is even, etc. Kinemetry is based on the assumption that for the odd moments the profile along the ellipse satisfies a simple cosine law, while for the even moments the profile is constant (the same assumption is also used in surface photometry). Kinemetry derives such best-fitting ellipses and analyses the profiles of the moments extracted along these by means of harmonic decomposition. It follows from this that the application of kinemetry on even moments is equivalent to surface photometry resulting in the same coefficients for parameterisation of the structures (e.g position angle, ellipticity and fourth order harmonics).

Application of kinemetry on odd maps such as velocity maps[1] provides radial profiles of the kinematic position angle PA_{kin}, axis ratio or flattening, q_{kin}=b/a (where b and a are lengths of minor and major axis, respectively), and odd harmonic terms obtained from the Fourier expansion (since velocity is an odd map, even terms are, in principle, not present, while in practice are very small and usually negligible). In the case of stellar velocity maps, the dominant kinemetry term is $k_1 = \sqrt{a_1^2 + b_1^2}$, representing the velocity amplitude, where a_1 and b_1 are the first sine and cosine terms, respectively. The deviations from the assumed simple cosine law are given by the first higher order term that is not fitted, $k_5 = \sqrt{a_5^2 + b_5^2}$, usually normalised with respect to k_1. These four parameters form the basis of our analysis because they quantify the kinematical properties of the observed galaxies: orientation of the map (a projection of the angular momentum), opening angle of the iso-velocity contours, the amplitude of the rotation and the deviation from the assumed azimuthal variation of the velocity map. For the other moments of the LOSVD one could derive similar quantities, depending on the parity of the moment. As will be discussed below, we focus on kinemetry coefficients that describe velocity maps in detail and some specific kinemetry coefficients from the maps of the higher order moments. A detailed description of the method, error analysis and parameters is given in Krajnović et al. (2006).

3.2 Radial profiles

Kinemetric radial profiles can be obtained along ellipses of different axial ratios and position angles. At each radius there is the best fitting ellipse, along which a profile of the kinematic moment will have a certain shape: it follows a cosine or it is constant, for odd

[1] It is customary in the literature to refer to the maps of mean velocity as *velocity fields*. Sometimes, due to the specific shape of contours of constant velocities, velocity maps are referred to as *spider diagrams* (e.g. van der Kruit & Allen 1978). Two-dimensional representations of the next moment are, however, usually referred to as velocity dispersion maps. Instead of alternating between *fields* and *maps* we choose to call all two-dimensional representations of the LOSVD maps: velocity map, velocity dispersion map, h_3 map....

and even moments, respectively. If this is the case, the higher order Fourier terms are non-existent or at least negligible for such an ellipse.

In the case of even moments, the best fitting ellipses describe the underlying iso-contours, like isophotes in the case of surface photometry, or contours of constant velocity dispersion, iso-σ contours. In the case of odd moments, this is somewhat more difficult to visualise, but the axial ratio of the best-fitting ellipse is related to the opening angle of the iso-velocity contours: the larger the axial ratio, the more open is the spider diagram of the velocity map.

In this study, kinemetry is used for extraction of parameters in the following ways:

i) We apply kinemetry to SAURON reconstructed images of galaxies, which are obtained by summing the spectra along the spectral direction at each sky position. This is equivalent to low resolution surface photometry on galaxies from the sample. We focus on the photometric position angle PA_{phot} and photometric axial ratio, related to ellipticity as q_{phot}=1-ϵ. In this case, kinemetry is used in its *even* mode, where even harmonics are fitted to the profiles extracted along the best fitting ellipses.
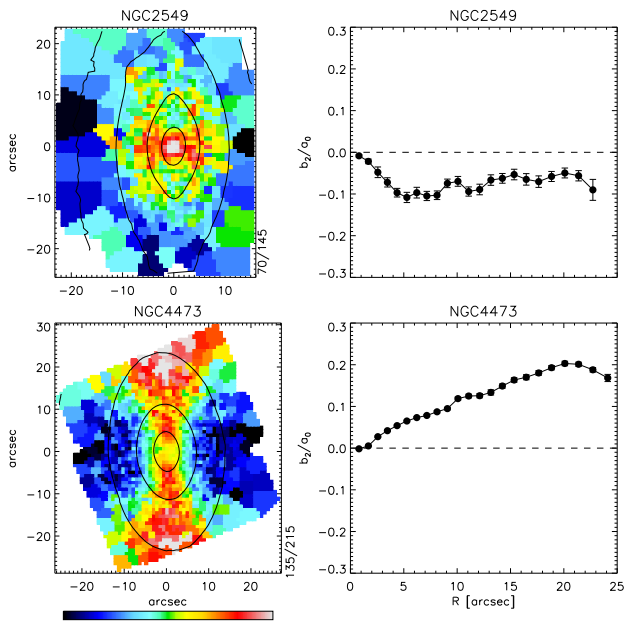
ii) We use kinemetry to derive radial profiles of the four parameters that describe velocity maps: PA_{kin}, q_{kin}, k_1 and k_5. In this case, kinemetry is applied to the maps in its *odd* mode, when only odd Fourier harmonics are fit to the profiles extracted along the best fitting ellipses, which are, in general, different from the best fitting ellipse of *(i)*. In some cases when it is not possible to determine the best-fitting ellipse we run kinemetry on circles (see below).

iii) Kinemetry is applied to velocity dispersion maps, using the *even* mode as in *(i)*. In this case, however, the parameters of the ellipses used to extract profiles were fixed to the best fitting values of surface photometry obtained in *(i)*.

iv) Maps of Gauss-Hermite coefficients h_3 and h_4 were also parameterised using kinemetry in *odd* and *even* mode, respectively. In both cases, we used the best fitting ellipses from the lowest *odd* (velocity map) and *even* moment (reconstructed image), respectively.

Before proceeding it is worth explaining in more detail our decision not to use kinemetry to fit the ellipses in some cases. Under *(ii)* we mentioned that on some velocity maps it was necessary to run kinemetry on circles. In general, the mean stellar velocity has an odd parity, and its map, in an inclusive triaxial case, will be point-antisymmetric. Certain maps, however, do not follow this rule, having no detectable net rotation, e.g. NGC4486, or the inner part of NGC4550. In the latter case, the zero velocity in the inner part can be explained by the superposition of two counter-rotating stellar components as advocated by Rubin et al. (1992) and Rix et al. (1992), where the mass of the counter-rotating component is about 50% of the total mass (Paper X). In other cases the non rotation could be a result of dominant box orbits which have zero angular momentum. The basic assumption of kinemetry for odd kinematic moments therefore breaks down resulting in velocity maps that appear noisy and one cannot expect reasonable results.

In practice, this means that the best-fitting ellipse parameters for maps without net rotation will not be robustly determined (degeneracy in both PA_{kin} and q_{kin}) while the higher harmonic terms will be large and meaningless. Specifically, k_5 will have high values. We partially alleviate this degeneracy by first running an unconstrained kinemetry fit on stellar velocity maps and identifying maps where $k_5/k_1 > 0.1$ and corresponding radii where it occurs. At these radii we re-run kinemetry, but using circles for extraction of velocity profiles and Fourier analysis. In this way we set the axial ratio q_{kin}=1 in order to break the degeneracy. Although the k_5/k_1

ferent amplitudes to the harmonic terms. Specifically, b_2 (cosine) term will be the most influenced, because this term is related to the error in the axial ratio (Jedrzejewski 1987), and the shapes such as in NGC2549 and NGC4473 will give negative (iso-σ rounder than isophotes) and positive (iso-σ flatter than isophotes) b_2, respectively. An alternative way to visualise the difference between these two maps based on the values of b_2 is to consider that a negative b_2, corresponds to a decrease of the σ at the major axis of the best fitting ellipse compared to the σ measured at the minor axis of the best fitting ellipse (NGC2549). In contrast, a positive b_2 corresponds to an increased value of the σ at the major axis position of the best fitting ellipse (NGC4473). By monitoring these harmonic terms it is possible to quantify the shape difference between the observed zeroth and second moments of the LOSVD.

3.3 Definition of structures on stellar velocity maps

A few kinematric profiles are able to describe a wealth of information from the maps. Specifically, we wish to use them to highlight the kinematic structures on the maps and to recognise hidden kinematic components. Here we present a set of quantitative criteria for describing features on the stellar velocity maps. Some of the criteria are dependent on the quality of the data and they should be modified if used on maps obtained with other IFUs. The following rules were presented by Krajnović et al. (2006) and Paper IX, but here we list them for the sake of clarity.

A single velocity map can contain a number of kinematic components. Often they are easily recognisable by visual inspection. In a quantitative way we differentiate between:

- *Single Component* (SC) map: having a radially constant or slow varying PA_{kin} and q_{kin} profiles.
- *Multiple Component* (MC) map: characterised with an abrupt change in either: $\Delta\mathrm{q}_{kin} > 0.1$, or $\Delta\mathrm{PA}_{kin} > 10°$, or a double-hump in k_1 with a local minimum in between, or a peak in k_5 where $k_5/k_1 > 0.02$.

MC maps are clearly more complex than SC maps. The above values for changes to the kinematric coefficients are used to determine the extent of each subcomponent (components C_1, C_2 and C_3 with radii R_{12} and R_{23} between them). Each subcomponent can be described as being of the following type (limiting values apply for the SAURON dataset):

- *Disc-like rotation* (DR): defined when the higher order harmonic $k_5/k_1 < 0.02$, while the variation of q_{kin} and PA_{kin} is less than 0.1 and 10°, respectively. Note that this name *does not* imply that the object is a disk intrinsically .
- *Low-level velocity* (LV): defined when the maximum of k_1 is lower than $15\ \mathrm{km\,s^{-1}}$. A special case is *Central low-level velocity* (CLV) when LV occurs in the central kinematical component on the map.
- *Kinematic misalignment* (KM): defined when the absolute difference between the photometric PA_{phot} and kinematric position PA_{kin} angles is larger than 10°.
- *Kinematic twist* (KT): defined by a smooth variation of the kinematics position angle PA_{kin} with an amplitude of at least 10° within the extent of the kinematic component.
- *Kinematically decoupled component* (KDC): if there is an abrupt change in PA_{kin}, with a difference larger than 20° between two adjacent components, or if there is an outer LV component (in which case the measurement of PA_{kin} is uncertain). A special case

Figure 1. Left: Voronoi binned stellar velocity dispersion maps of NGC2549 (top) and NGC4473 (bottom). Over-plotted lines are isophotes. In the lower right corner of each map are values that correspond to minimum and maximum colours on the colour bar. **Right:** Radial profiles of b_2/a_2 kinemetry terms for NGC2549 (top) and NGC4473 (bottom).

term cannot be directly compared with the k_5/k_1 term obtained from a best-fitting ellipse, in this case, if there is any indication of odd parity in the map, we can still determine the local amplitude of rotation k_1, and give a good estimate for PA_{kin}.

The other note refers to items *(iii)* and *(iv)*. Although, in principle, it would be possible to run kinemetry freely on the velocity dispersion maps, or maps of higher Gauss-Hermite moments (e.g. h_3 and h_4), the noise in the data is too high to give trustworthy results for the whole sample. By setting the shape of the curve to the best-fitting ellipses of the corresponding lowest odd or even moment, the harmonic terms of kinemetry quantify the differences between these even and odd moments of the LOSVD.

An example of expected differences can be visualised comparing the isophotes of the surface brightness and the stellar velocity dispersion maps of NGC2549 and NGC4473 (Fig. 1). On both images isophotes are aligned with the vertical (y) axis of the maps. In the case of NGC2549 the contours of constant velocity dispersion seem to be perpendicular to the isophotes, at least within the central $10''$, while in the rather unusual case of NGC4473, the high values of velocity dispersion have the same orientation as the isophotes. The physical explanation of these striking differences should be looked for in the internal orbital structure. We postpone this discussion to Section 4.4.

The noise and irregular shape of iso-σ contours decrease the usefulness of fitting for the velocity dispersion contours. Extracting harmonic terms along the isophotes, however, can yield a clear signal of the different shape of these two moments. An extracted velocity dispersion profile in these two cases (for example along the second brightest isophote shown on Fig. 1) will go through two maxima and two minima. The minima and maxima of these two profiles will be out of phase, because along the major axis in NGC2549 there is a decrease in velocity dispersion while in NGC4473 there is an increase. The decomposition of these two profiles will give dif-

of KDCs are *Counter rotating cores* (CRC) where $\Delta\mathrm{PA}_{kin}$ between the components is $180°$ (within the uncertainties).

Most of the above definitions are new, arising from two-dimensional maps which offer a more robust detection of structures. The definition of KDC is, however, similar to the one used in the past (e.g. Bender 1988a; Statler 1991), where the two-dimensional coverage enables a determination of the orientation of the kinematic components. It should be noted that classification of a kinematic component as a CLV is strongly dependent on the spatial resolution of the instrument. As will be seen later, higher spatial resolution can change the appearance and therefore the classification of the components.

Similarly, it should be stressed that the limiting values used for these definitions are geared towards the SAURON data. The OASIS data, due to different instrumental properties and observing set-up, will have somewhat different limiting values, mostly arising in the higher order Fourier terms. For example, the mean uncertainty of k_5/k_1 term for the OASIS sample is 0.033, significantly higher compared to the one for the SAURON sample (0.015). In order to treat consistently the two data sets, we adopt a somewhat more conservative value of 0.04 as the limiting values for k_5/k_1 in definition of DR component when estimated from the OASIS data.

While abrupt changes in the orientation, axial ratio, or velocity amplitude are intuitively clear as evidences for separate kinematic components, the k_5/k_1 as an indicator of components is more complex to comprehend. Still, the simple models of two kinematic components rotating at a given relative orientation give rise to k_5/k_1 term in the kinematic expansion in the region where these components overlap (Krajnović et al. 2006). Since we measure luminosity weighted velocities, the position and extent of the raised k_5/k_1 region depends on relative luminosity contributions of the components, marking the transition radii between the components and not their start or end. Furthermore, it is also, necessary, to distinguish between high k_5/k_1 due to a super-position of kinematic components (a genuine signal) and high k_5/k_1 originating from noisy maps, such as maps with no detectable rotation (e.g. NGC4486) or large bin-to-bin variations (e.g. OASIS map of NGC3379). For our data, when the signal in k_5 is 10% of k_1, we consider the noise too high and the k_5/k_1 ratio not usable for detecting individual components.

3.4 Seeing and quantification of kinematic components

Robust estimates of the number of sub-components in velocity maps and their sizes are influenced by three major factors: data quality, physical properties and seeing. While the data quality is described by measurement uncertainties, and in that sense it is quantifiable to some extent, the other two factors are more complex. By 'physical properties' we assume physical processes that hide kinematic information from our view, such as specific orientation of the object, dust obscuration or simply the fact that we are measuring luminosity weighted quantities and we might miss kinematic components made up of stars that constitute a low luminosity fraction of the total population.

The influence of seeing is particularly relevant for subcomponents in the centres of galaxies. In Appendix A we tested the dependence of the kinematic coefficients on representative seeings, for velocity maps viewed at different orientations. This exercise showed that: *(i)* PA_{kin} and k_5/k_1 are not significantly influenced by the seeing, *(ii)* the amplitude and, to a minor extent, the shape of k_1 are somewhat influenced by the seeing, and *(iii)* the axial ratio

q_{kin} can be strongly influenced by the seeing (Fig. A2). In addition to these conclusions, the test showed that the inclination of an object is also a factor contributing to the change of the intrinsic q_{kin}, and to a minor extent, k_1 profiles, where higher inclinations are particularly influenced by the seeing effects.

In practice, this means that the change in q_{kin} is a less robust indicator of kinematic components. We found that more robust indicators are abrupt changes in k_5/k_1 and PA_{kin} profiles, double humps in k_1 profiles or decrease of k_1 amplitude below our detection limit for rotation. We used these as estimates of the sizes of kinematic components. It should be, however, noted that the size of a component is just a luminosity weighted estimate, originating from a super-position of luminosities of individual components, and the component can intrinsically extend beyond that radius. Only detailed dynamical models could give a more robust estimate of the internal orbital structure.

3.5 Determination of global and average values

In addition to radial profiles we present in this paper a number of average quantities. Similar luminosity-weighted quantities have already been derived in Papers IX and X: global PA_{kin}, global PA_{phot}, average ϵ. In this study we use the velocity maps to determine the luminosity weighted average $\langle\mathrm{PA}_{kin}\rangle$, $\langle q_{kin}\rangle$, and $\langle k_5/k_1\rangle$ for the whole map and for each kinematic component. We also measured the luminosity weighted $\langle\mathrm{PA}_{phot}\rangle$, $\langle q_{phot}\rangle$ from the reconstructed images (both global and for each component), $\langle b_2/a_0\rangle$ from velocity dispersion maps and average values of h_4 (measured as the a_0 harmonic term) from h_4 maps. In practice, we do this following the expression from Paper IX. The mean $\langle G\rangle$ of a quantity $G(R)$ derived from its sampled radial profiles can be approximated with:

$$\langle G\rangle \sim \frac{\sum_{k=1}^{N} q(R_k)F(R_k)G(R_k)(R_{out,k}^2 - R_{in,k}^2)}{\sum_{k=1}^{N} q(R_k)F(R_k)(R_{out,k}^2 - R_{in,k}^2)} \tag{1}$$

where $q(R_k)$ and $F(R_k)$ are the axial ratio and the surface brightness of the best fit ellipse, with semi-major axis R_k. Eq. (1) is based on an expression defined in Ryden et al. (1999). The uncertainties of these average values are calculated in the standard way as the sum of the quadratic differences between the average value and the value at each position R_k.

In Paper X the global PA_{kin} was derived using the formalism from Appendix C in Krajnović et al. (2006). This approach differs from the one described here in the sense that it is less sensitive to the kinematic structures in the central region, such as abrupt changes of PA in case of a KDC. That approach is well suited for making global comparisons between PA_{kin} or PA_{phot}, such as global kinematic misalignment, when it is required that they are measured on large scales to avoid influence of local perturbations in the nuclear regions (e.g. seeing, dust, bars). In this study, however, we want to compare the radial properties of different moments of the LOSVD and for that reason we use the approach of Paper IX to all measured quantities. Note that for the purpose of the direct comparison we measured both kinematic and photometric quantities on the SAURON data, in contrast with Papers IX and X.

4 RESULTS

In this section we present the results of kinematic analysis of the LOSVD moments maps. We look at the presence of kinematic substructures in velocity maps (Section 4.1), properties of radial pro-

files of PA_{kin}, k_1, σ (Section 4.2), comparison between q_{kin} and q_{phot} (Section 4.3), the shape difference between isophotes and iso-σ contours (Section 4.4) and properties of h_3 and h_4 Gauss-Hermite moments (Section 4.5) with the purpose to investigate the internal structure of SAURON galaxies. Kinemetry probes local characteristics of galaxies, and we wish to link those with the global properties described in Papers IX and X. In this analysis, the most useful is the first moment of the LOSVD, the mean velocity, because it is a moment rich in structure and with the strongest signal. We present the kinemetric profiles of this moment in Appendix B. Although kinemetry is performed on other moments of the LOSVD, we discuss the dominant terms only.

4.1 Substructures on the velocity maps

Looking at the kinemetric profiles of 48 SAURON galaxies (Fig. B1) the following general conclusions can be made:

- PA_{kin} profiles are in general smooth and often constant (e.g. NGC2974) or mildly varying (e.g. NGC474). In some cases there are abrupt changes of up to $180°$ within $1 - 2''$ (e.g. NGC3608).
- Profiles of the axial ratio q_{kin} are generally smooth and often similar to q_{phot} profiles (e.g. NGC1023, NGC3384, NGC4570).
- There is a variety of k_1 profiles, most of them rise and flatten, but some continue to rise, while some drop (e.g. NGC4278, NGC4477 and NGC4546).
- Considering the k_5/k_1 radial dependence, there are three kinds of objects: those that have the ratio below 0.02 along most of the radius (e.g. NGC2974), those that have the ratio greater than 0.1 along most of the radius (e.g. NGC4374) and those that have the ratio below 0.02 with one (or more) humps above this value (e.g. NGC2549).
- Objects with $k_5/k_1 > 0.1$ along a significant part of the profile from SAURON data are all classified as slow rotators in Paper IX (e.g. NGC4486).

A further step in understanding the complex velocity maps can be made by applying definitions of kinemetric groups (see Section 3.3) to the radial profiles. They are summarised in Table 1. There are 15 galaxies characterised as SC $(31\%)^2$, the rest being MC galaxies (69%) of which 10 have KDC (21%) and 4 CLV (8%). Higher resolution observations with OASIS, however, show that all SAURON CLVs are in fact small KDCs and, moreover, CRCs (Paper VIII). This means that there are actually 14 (29%) KDCs in the SAURON sample. Kinematic profiles of the OASIS data also clearly show structures that are partially resolved in the SAURON observations, such as KDC (NGC4621, NGC5198, NGC5982) or co-rotating components which often have larger amplitudes of rotation in the OASIS data, corresponding to the nuclear disks visible on the HST images. The effects of specific nuclear kinematics, related mean ages of the components and possible different formation paths were previously discussed in Paper VIII.

In addition to this grouping of the velocity maps, we can also describe the kinematic components. Out of 15 SC galaxies, 8 are DR (53%), 2 are KT (13%) and 4 are LV (27%), while the remaining galaxy (NGC2768) is a rather special case of a solid body rotator (see below). The majority of MC galaxies have only two kinematic components (30 or 91%), but there are some with three kine-

---

^{2} Although NGC4550 is made of two counter-rotating and co-spatial disks (Section 3.2), it is formally characterised as a SC galaxy due to its low velocity within the SAURON FoV.
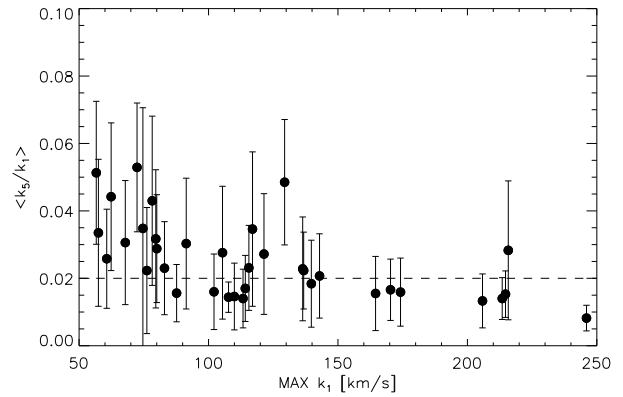
Figure 2. A relation between the maximum amplitude of rotation and luminosity-weighted average of k_5/k_1 ratio, which measures departures from the cosine law for velocity profiles extracted along the best fitting ellipse. All points belong to fast rotators.

matic components (3 or 9%). Many of the components are similar in properties. If the inner component (C_1) is DR then the second component (C_2) is also a DR. If C_1 has a more complex kinematic structures (KDC, LV, KT), C_2 or C_3 will in most cases still be a DR. Exceptions are found in a few cases when C_2 is not rotating and can be described as LV. In some cases components may show KT, but their k_5/k_1 ratio is less than or equal to 0.02. Counting all galaxies that have at least one component with $k_5/k_1 \lesssim 0.02$, the number of systems with DR-like characteristics rises to 35 (73%). In terms of E/S0 classification, this means that 74% of Es and 92% of S0s have components with disk-like kinematics

Using the resolving power of the OASIS data we can go even further: allowing for large error bars and allowing for considerable uncertainty of component boundaries, virtually every galaxy that shows rotation (including parts of KDCs) has at least one region with $k_5/k_1 \lesssim 0.02$ (0.04 in OASIS). This can be seen on Fig. 2 that shows luminosity weighted average of k_5/k_1 ratio versus the maximum rotational amplitude k_1 for all fast rotators measured on the SAURON data. The large uncertainties in some cases reflect the multiple component nature of fast rotators, because k_5/k_1 ratio rises in the transition region between components (Krajnović et al. 2006). Notably, both average values and uncertainties rise as the maximum rotation velocity decreases. This suggest a more complex structure (more components, larger difference between components) in galaxies with lower amplitude of rotation.

We estimated local kinematic misalignment for each kinematic component. The results show that a total of 25 galaxies (52% of the sample) have some evidence of KM. It should, however, be kept in mind that it is difficult to determine the sense of rotation for LV components. Ignoring galaxies with a LV in the single component or in the second component, we are left with 15 galaxies with kinematic misalignments. Of these, 13 galaxies show misalignment in the first component, and 7 in the second component. Moreover, only 5 galaxies show misalignment in two components, as a global property within the SAURON field of view.

As it can be seen from the kinemetric profiles there are special cases for which kinemetry is not able to determine the characteristic parameters robustly. This, in general, occurs when velocity drops below $\sim 15 \ km \, s^{-1}$ (e.g. NGC4486, NGC4550), and it is not surprising since these maps also often lack odd parity, an expected property of the first moment of the LOSVD. As discussed

Table 1. Kinemetric properties of the 48 E and S0 SAURON galaxies.

Galaxy (1)	Group (2)	N_C (3)	R_{12} (4)	R_{23} (5)	C_1 (6)	C_2 (7)	C_3 (8)	KM (9)	Rotator (10)	Comment (11)
NGC0474	MC	2	7	–	DR	DR	–	KM(1,2)	F	KT between C_1 and C_2
NGC0524	SC	1	–	–	DR	–	–	–	F	Possible C_2 beyond r=12″
NGC0821	SC	1	–	–	DR	–	–	–	F	Flat k_1 profile
NGC1023	SC	1	–	–	KT	–	–	–	F	$k_5/k_1 < 0.02$,
NGC2549	MC	2	13	–	DR	DR	–	–	F	C_2: Flat k_1 profile
NGC2685	SC	1	–	–	DR	–	–	–	F	–
NGC2695	MC	2	7	–	DR	DR	–	–	F	–
NGC2699	MC	2	6	–	DR	DR	–	KM(1,-)	F	C_2: Flat k_1 profile
NGC2768	SC	1	–	–	–	–	–	–	F	$r \lesssim 10″$ rigid body rotation; $k_5/k_1 < 0.02$ for $r > 10″$
NGC2974	SC	1	–	–	DR	–	–	–	F	–
NGC3032	MC (CLV)	2	2.5	–	LV	DR	–	–	F	CRC in OASIS map
NGC3156	SC	1	–	–	DR	–	–	–	F	–
NGC3377	SC	1	–	–	KT	–	–	–	F	$k_5/k_1 < 0.02$ over the map
NGC3379	SC	1	–	–	DR	–	–	–	F	–
NGC3384	MC	2	10	–	DR	DR	–	KM(-,2)	F	–
NGC3414	MC (KDC)	2	10	–	DR	LV	–	KM(-,2*)	S	CRC
NGC3489	MC	2	6	–	DR	DR	–	–	F	-
NGC3608	MC (KDC)	2	10	–	DR	LV	–	KM(-,2*)	S	CRC
NGC4150	MC (CLV)	3	3.5	9.5	LV	–	DR	KM(1,-,-)	F	KDC in OASIS map with $r_{size} = 1″5$
NGC4262	MC	2	9	–	DR	–	–	KM(1,2)	F	–
NGC4270	MC	2	6	–	–	–	–	–	F	Possible there components
NGC4278	MC	2	16	–	DR	–	–	KM(-,2)	F	C_2: Decreasing k_1 profile
NGC4374	SC	1	–	–	LV	–	–	KM*	S	-
NGC4382	MC (CLV)	3	2	14.5	LV	DR	DR	KM(1,-,-)	F	CRC in OASIS map, KT between C_1 and C_2
NGC4387	MC	2	7	–	DR	DR	–	–	F	Decreasing k_1 beyond $r = 13″$
NGC4458	MC (KDC)	2	3	–	–	LV	–	KM(-,2*)	S	–
NGC4459	MC	2	12	–	DR	DR	–	KM(1,-)	F	–
NGC4473	MC	2	10	–	DR	–	–	–	F	C_1: possible KT. C_2: decreasing k_1 profile.
NGC4477	SC	1	–	–	DR	–	–	KM	F	–
NGC4486	SC	1	–	–	LV	–	–	KM*	S	–
NGC4526	MC	2	11	–	DR	–	–	–	F	C_2: decreasing k_1 profile
NGC4546	MC	2	9	–	DR	DR	–	KM(1,-)	F	C_2: Flat k_1 profile
NGC4550	SC	1	–	–	LV	–	–	KM*	S	Two co-spatial counter-rotating disks not detected
NGC4552	MC (KDC)	2	4	–	KT	–	–	KM(1,2)	S	Flat $k_1 = 15\,\mathrm{km\,s^{-1}}$ over the map
NGC4564	SC	1	–	–	DR	–	–	–	F	–
NGC4570	MC	2	8	–	DR	DR	–	–	F	–
NGC4621	MC (KDC)	2	4	–	DR	DR	–	KM(1,-)	F	CRC in OASIS with r∼ 1″5
NGC4660	MC	2	7	–	DR	DR	–	–	F	–
NGC5198	MC (KDC)	2	2.5	–	–	KT	–	KM(1*,2*)	S	C_2: LV between 2.5-10″
NGC5308	MC	2	7	–	DR	DR	–	–	F	No signature of C_2 in k_5/k_1
NGC5813	MC (KDC)	2	12	–	DR	LV	–	KM(-,2*)	S	–
NGC5831	MC (KDC)	2	8	–	DR	LV	–	KM(-,2*)	S	–
NGC5838	MC	2	6	–	DR	DR	–	–	F	No signature of C_2 in k_5/k_1
NGC5845	MC	2	4.5	–	DR	DR	–	–	F	–
NGC5846	SC	1	–	–	LV	–	–	KM*	S	–
NGC5982	MC (KDC)	2	3.5	–	–	LV	–	KM(1,-)	S	C_2: LV is between 2-8″
NGC7332	MC (KDC)	3	3	12	KT	DR	DR	KM(1,-,-)	F	C_2: continuously increasing k_1; KDC only in PA change
NGC7457	MC (CLV)	2	3	–	KT	DR	–	KM(1,2)	F	C_2: continuously increasing k_1

Notes: (1) Galaxy identifier; (2) Kinematic galaxy group: see text for details; (3) Number of kinematic components; (4) Transition radius between the first and second components (arcsec); (5) Transition radius between the second and third components (arcsec); (6), (7) and (8) Kinematic group for the first second and third components; (9) Local kinematic misalignment between luminosity-weighted averages of PA_{kin} and PA_{phot}: numbers refer to the kinematic component and * notes that the PA_{kin} was determined in the region with k_1 mostly below $15\,\mathrm{km\,s^{-1}}$; (10) Rotator class: S – slow rotator, F – fast rotator (11) Comment.

in Krajnović et al. (2006), another exception is the case of solid body rotation for which the iso-contours are parallel with the zero-velocity curve. In the SAURON sample this is seen in NGC2768. Since the velocity iso-contours are parallel the axial-ratio and the position angle are poorly defined and in practice strongly influenced by noise in the data. Determination of the best-fit ellipse parameters for the solid body rotation is degenerate. From these reasons this galaxy should also be considered with care when comparing with kinemetry results for other objects.

4.2 Fast vs Slow Rotators

As stated above, all galaxies with $k_5/k_1 > 0.1$ along a significant part of the profile from SAURON data are classified as slow rota-

tors in Paper IX. To some extent this is expected since slow rotators in general show very little rotation and kinematry assumptions are not satisfied. The origin of the noise in the maps of slow rotators, which generates large k_5/k_1, is likely reflecting a special internal structure, and, in principal, does not come from technical aspects of the observations. Even velocity maps with low amplitude of rotation could show regular spider diagrams (e.g. disks seen at very low inclinations) observed at the same signal-to-noise. The one-to-one relation between slow rotators and objects with large higher-order harmonic terms is significant since the slow/fast rotator classification is based on both velocity and velocity dispersion maps and reflects the internal structure.

The OASIS data cover only a small fraction of the effective radius and do not show this relationship. The slow rotators NGC3414, NGC3608, NGC5813 and NGC5982 show considerable rotation because the KDC is covering the full OASIS FoV, while the central regions of the fast rotators NGC2768, NGC3032 and NGC3379 still have small amplitudes of rotation and high (and noisy) k_5/k_1 ratios.

The velocity maps of the 12 slow rotating galaxies in our sample can be described either as LV or as KDC+LV. In that respect, 4 slow rotators are SC systems (NGC4374, NGC4486, NGC4550 and NGC5846) which do not show any detectable rotation (at SAURON resolution) and the other 8 are MC systems where C_1 is a KDC and C_2 is a LV. In between these two cases is NGC4552 with a rather constant rotation velocity of 15 km s^{-1}, the boundary level for LV, and the C_1 between a KDC and a large KT. The other three quarters of galaxies in the SAURON sample are fast rotators. Only a third of them are described as SC, but as shown above (Section 4.1) all fast rotators have components with kinematics that can be described as DR. Moreover, in the case of some slow rotators with small, but not negligible rotation in the centres (KDC), the higher resolution OASIS data were able to ascertain that these components have near to DR properties (within often large uncertainties)

Figure 3 has three panels highlighting most obvious kinematic properties of slow and fast rotators. The top panel shows radial variations of the kinematic position angles, PA$_{kin}$, which are present in various forms, ranging from minor twists in the nuclei, through abrupt jumps at the end of KDCs, to almost random changes with radius. However, only PA$_{kin}$ of slow rotators are characterised by strong and rapid changes. Fast rotators show remarkably constant PA$_{kin}$. If twists are present in PA$_{kin}$ of fast rotators, they are small in amplitude ($\lesssim 30°$) and confined to the nuclear region in shapes of physically small KDCs (NGC4150, NGC4382, NGC4621, NGC7332, NGC7457). Slow rotators on the other hand show a much greater amplitude in change of PA$_{kin}$.

It should be stressed again that determination of PA$_{kin}$ for slow rotators is much more ill defined than for fast rotators in the sense that if there is no rotation, there is also no orientation of rotation. The abrupt changes in PA$_{kin}$ are the consequence of this in some cases (NGC4374, NGC4486, NGC4550, NGC5846), and while one could debate the robustness of measured PA$_{kin}$, one should acknowledge the different nature of these systems from objects with a constant PA$_{kin}$.

The difference between the slow and fast rotators is most visible in the amplitude of rotation. The middle panel of Figure 3, shows the radial profiles of k_1 kinematric terms for 48 early-type galaxies. Most of the profiles cover up to 1 R_e in radius. Slow rotating galaxies can show a non-zero amplitude of rotation in the centres (KDCs), but the amplitude is, in general, not very high and towards the edge of the map it is mostly negligible. The only ex-
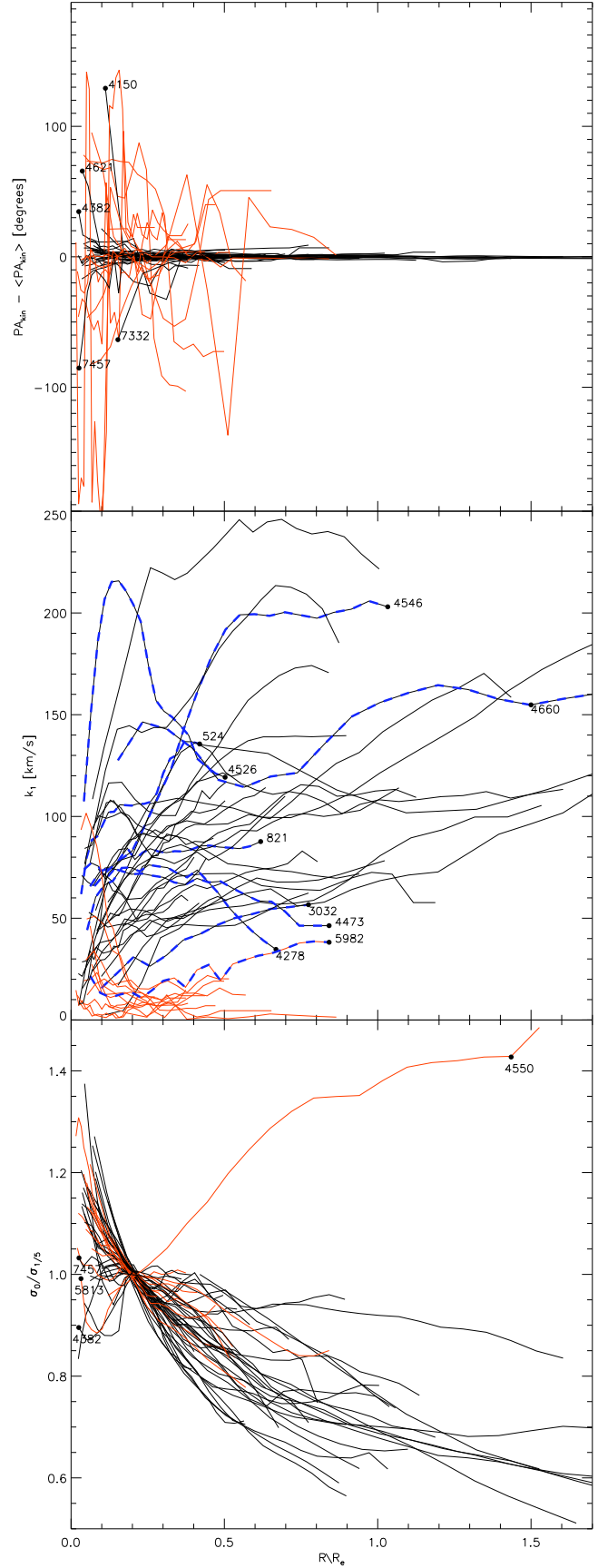
Figure 3. Radial profiles of (from top to bottom) PA$_{kin}$- $\langle$PA$_{kin}\rangle$, k_1 and σ_0 from the SAURON data. $\langle$PA$_{kin}\rangle$ are luminosity weighted averages of PA$_{kin}$ profiles. σ_0 profiles are normalised at $R_e/5$. The profiles of slow and fast rotators are coloured in red and black, respectively. In the middle panel dashed blue lines are over-plotted to guide the eye for the cases with specific profiles as mentioned in text.

ception is NGC5982, which approaches two fast rotators with the slowest rotation in the outer regions (NGC4278 and NGC4473).

Another characteristic of this plot is the variety of profiles. They include: monotonically rising profiles (e.g. NGC3032), profiles with an initial slow rise which turns to a more rapid one (e.g. NGC524), a rapid rise to a maximum followed by a plateau (e.g. NGC4546), rise to a maximum followed by a decrease (e.g. NGC4526), double hump profiles (e.g. NGC4660), flat profiles (e.g. NGC821) and, in slow rotators, profiles showing a decrease below our detection limit. Keeping in mind that the SAURON sample is not a complete sample, among fast rotators there are 17 (47%) with increasing profile at the edge of the SAURON map, 9 (25%) have flat profiles, 5 (14%) decreasing profiles and 4 galaxies have intermediate (difficult to classify) profiles. Among slow rotators there are 3 (25%) galaxies with increasing profiles at the edge of the map, the rest being flat and below the detection limit.

These statistics are influenced by the size of velocity maps and the coverage of kinematics components by kinematic ellipses. Clearly, larger scale observations would detect the end of rise in amplitude in galaxies that are now observed to have increasing k_1. Similarly, it is possible that a decrease in k_1 could be followed by an additional increase or a flat profile at large radii. Still, there are two general conclusions for fast rotators: they mostly show increasing velocity profiles at $1R_e$, where the range of maximum velocity amplitude spans 200 km s^{-1}. On the other hand, slow rotators have velocity amplitude mostly less than 20 km s^{-1} at $1R_e$.

The bottom panel of Fig. 3 shows radial velocity dispersion profiles, σ_0, extracted along the isophotes from the velocity dispersion maps as a_0 harmonic terms. All profiles are normalised to their value at $R_e/5$. This highlights the similar general shape of the σ_0 radial profiles. The only outlier is NGC4550 with an σ_0 profile which increases with radius. Most of the other profiles, while different in detail, show a general trend of increasing σ_0 towards the centre and also have a similar shape. A few profiles are consistent with being flat ($\Delta\sigma_0/\Delta R \lesssim 30 \text{ km s}^{-1}$) over the whole profile (visible only in fast rotators such as NGC7457).

If there are any real differences between σ_0 profiles, they are apparent for radii smaller than $R_e/5$. There are a few exceptions to the general trend: *i)* profiles with a decrease of more than 5% in the normalised σ_0 within $R_e/5$ (e.g. NGC4382), *ii)* profiles that are flat to within 5% inside the $R_e/5$ (e.g. NGC7457), and *iii)* profiles with a central rise followed by a drop and consecutive rise forming a profile with double maxima (e.g. NGC5813). These cases occur mostly in fast rotators, with a few exceptions in slow rotators.

These central plateaus and drops are interesting, because classical theoretical work predicts that, for constant mass-to-light ratio, $r^{1/n}$ light-profiles have velocity dispersion minima in the centres of galaxies (Binney 1980; Ciotti & Lanzoni 1997), unless they contain central black holes (e.g. Merritt & Quinlan 1998). The central σ-drops evidently do not occur frequently in real early-type galaxies, but are, perhaps marginally more common to fast rotators. About 10% of the SAURON early-types exhibit the central drop (but additional 20% have flat central profiles), which is much less compared to 46% among the Sa bulges, also observed with SAURON data (Falcón-Barroso et al. 2006).

4.3 Distribution of axial ratios

We now compare average photometric and kinematic axial ratios of SAURON galaxies. The axial ratio of a velocity map is related to the opening angle of the iso-velocity contours. In other words, the pinching of the contours in a spider diagram is related to the axial

ratio of the best fitting ellipse given by kinemetry. As the kinematic axial ratio of slow rotators is an ill defined quantity (set to 1), in the rest of this section we focus on the average axial ratios of the fast rotators.

In Fig. 4 we compare values of $\langle q_{kin} \rangle$ and $\langle q_{phot} \rangle$ for fast rotating galaxies. Since the typical seeing for SAURON data ranges up to $2''.5$, we exclude the inner $5''$ of the q_{kin} profiles from our derivation of the luminosity weighted average values (Appendix A). The left hand panel shows a one-to-one correlation between the two quantities, although the scatter and uncertainties are large. The right hand panel shows more clearly the amount of scatter in these relations, as measured by the difference $\langle q_{kin} \rangle$ - $\langle q_{phot} \rangle$. The typical variation of the measured average Δq_{kin} is 0.1, as shown with vertical guidelines on the right panel. Outside this region there are about dozen galaxies. A few of these have $\langle q_{kin} \rangle$ larger than $\langle q_{phot} \rangle$; their photometric axial ratio is flatter than the kinematic, while the majority of outliers have the kinematic axial ratio flatter than the photometric. Let us consider in more detail only objects at significant distances from the vertical lines (i.e. $\langle qk \rangle - \langle qp \rangle > 0.15$): NGC821, NGC4270, NGC4473, NGC4621, NGC5308 and NGC5838.

If we look at the q_{kin} profiles of the three galaxies (Fig. B1) with $\langle q_{kin} \rangle > \langle q_{phot} \rangle$, we can see that some of their kinematic sub-components have axial ratios very similar to the local photometric axial ratios. Notably, in the case of NGC5308 this is the outer component, especially at radii near to the edge of the SAURON FoV. The middle range, where the differences are the largest, is also the region of the transition between the two kinematic components. The mixing of the components changes the measured $\langle q_{kin} \rangle$, but it should be also noted that the $\langle q_{phot} \rangle$ varies over the whole map, becoming flatter and similar to $\langle q_{kin} \rangle$ with radius. This is not the case in NGC4473. Here the photometric axial ratio remains constant, but the kinematic axial ratio changes at larger radii. Again this change occurs in the transition region between the two kinematic components. Detailed dynamical modelling of this galaxy shows that it is made of two counter-rotating stellar components of unequal mass. This object is physically similar to NGC4550, where the main difference is in the mass fraction of the two components (Paper X). In the case of NGC4270 it is the q_{phot} that steadily changes with radius, while q_{kin} has mostly high values, but shows abrupt changes between the points. These are related to sometimes rather high values of k_5/k_1, which also changes abruptly between the adjacent points, a behaviour originating from the noisy transition region between two kinematic components. Since it is hard to disentangle the noise from the genuine physical signal in q_{kin} measurement, and given the boxy appearance on the large scales, we note that this object could be a true and unusual outlier from the relation between q_{phot} and q_{kin}.

Galaxies with $\langle q_{kin} \rangle < \langle q_{phot} \rangle$ are either single component (NGC821 and NGC4621, if we exclude the CRC in NGC4621 of $\sim 4''$ in size) or multi component (NGC5838). The HST image of NGC5838 has a prominent nuclear dust disk with the axial ratio between $0.3 - 0.4$, constraining its inclination to about $70°$. It is possible that the velocity map is dominated by the presence of an associated stellar disk embedded in the galaxy body. NGC821 and NGC4621 were parametrised via the Multi-Gaussian Expansion (Emsellem et al. 1994; Cappellari 2002) in Paper IV. Both models required very flat Gaussians to reconstruct the light distribution (in both cases, the smallest axial ratios of the Gaussians of the MGE models were 0.3); these Gaussians are tracing disks embedded in spheroids. If we compare the $\langle q_{kin} \rangle$ with the flattest MGE Gaussians, both galaxies move well within the two vertical lines on right hand panel of Fig. 4 (blue lines).
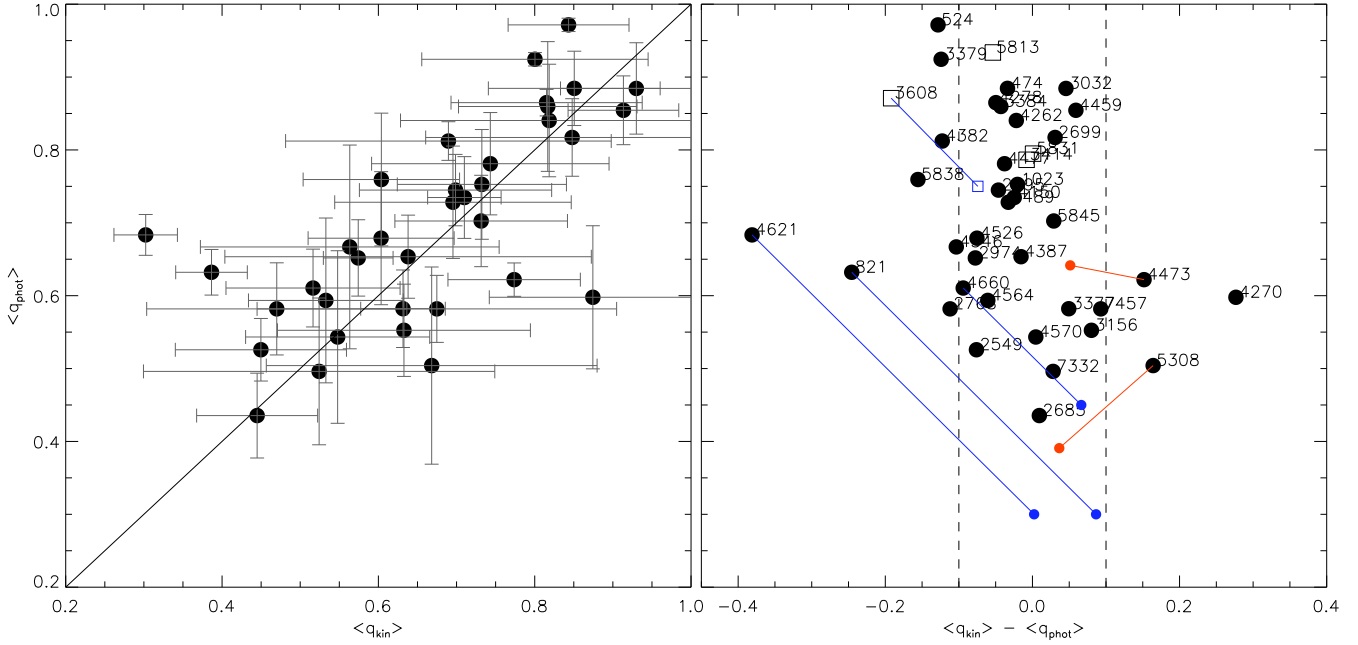
Figure 4. Left: Relation between luminosity-weighted kinematic and photometric axial ratios, $\langle q_{kin} \rangle$ and $\langle q_{phot} \rangle$, respectively, for fast rotating galaxies in the SAURON survey measured beyond $5''$ to avoid seeing effects. The black line is the 1:1 relation. The error bars describe the radial variations of q_{phot} and q_{kin} profiles. **Right:** Difference between luminosity-weighted kinematic and photometric axial ratios plotted against the photometric axial ratio. Dashed vertical lines represent a typical variation of q_{kin} profiles, which is the dominant uncertainty factor for comparison with q_{phot}. Solid symbols are fast rotating galaxies, while open squares are KDC components of slow rotators. The red lines between symbols link $\langle q_{kin} \rangle$ with $\langle q_{phot} \rangle$ measured on inner (NGC4473) and outer (NGC5308) kinematic components. The blue lines link $\langle q_{kin} \rangle$ and axial ratio of the MGE models.

As a matter of interest, on the same right hand plot of Fig. 4 we overplotted axial ratios for the big KDCs in the sample: NGC3414, NGC3608, NGC5813 and NGC5831. The shape of their kinematics is similar with the distribution of light, except in the case of NGC3608. Its KDC has flatter kinematics than the light, but the flattest MGE Gaussian is comparable with the kinematic axial ratio. This suggest that even some of the sub-components of the slow rotating galaxies have similar properties like fast rotating galaxies.

Having in mind that q_{kin} profiles can vary significantly with the radius, and the average values could be contaminated by the contribution of the transition regions between the components, we conclude that there is a near one-to-one correlation between average kinematic and photometric axial ratios in fast rotating galaxies, with a number of objects having $\langle q_{kin} \rangle < \langle q_{phot} \rangle$, and, hence, having disk-like components more visible in their kinematics than in photometry.

4.4 Shape differences between velocity dispersion and surface brightness maps

As shown in Section 3.2, the isophotes are not necessary a good representation of contours of constant velocity dispersion and the deviations are visible in the second cosine term (b_2) of the harmonic decomposition of the velocity dispersion profiles extracted along the isophotes. On Fig. 5 we quantify the differences between isophotes and iso-σ contours by plotting the normalised luminosity-weighted second term ($\langle b_2/a_0 \rangle_\sigma$) extracted along the isophotes of SAURON galaxies. Slow rotators are shown in red.

Focusing on the left hand panel, it is clear that galaxies in sample span a large range of $\langle b_2/a_0 \rangle_\sigma$, both positive and negative. If we exclude NGC4473 and NGC4550, there is a tail of galaxies

with negative values up to ~ -0.1. Also, it seems that there is a trend of high negative $\langle b_2/a_0 \rangle_\sigma$ in flat galaxies: as galaxies become rounder, $\langle b_2/a_0 \rangle_\sigma$ tends to zero; above $\langle q_{phot} \rangle = 0.8$ galaxies have small absolute value of $\langle b_2/a_0 \rangle_\sigma$. Slow rotators are relatively round systems (Paper X) with $q_{phot} > 0.7$ (excluding the special case of NGC4550). Their $\langle b_2/a_0 \rangle_\sigma$ values are small and mostly positive. Typical measurement error of $\langle b_2/a_0 \rangle_\sigma$ is ~ 0.03, and hence, the slow rotators are consistent with having velocity dispersion maps very similar to the the distribution of light, with possibly marginally flatter iso-σ contours.

Before we turn to the right panel on Fig. 5, let us go back to Fig. 1 and the example of NGC2549 and NGC4473. Their stellar velocity dispersion maps have different shapes from the distributions of light, but they have similar absolute values of $\langle b_2/a_0 \rangle_\sigma$; they fall on the opposite sides of Fig. 5. There is, however, evidence that in both cases the deviations from the photometry have similar physical origin. NGC2549 shows clear photometric and kinematic evidence for a stellar disk viewed at a high inclination (Fig. B1). The velocity dispersion map has a very specific 'bow-tie' shape in the central $10''$, while outside its amplitude is low everywhere. The 'bow-tie' shape can be explained with a light-dominating dynamically cold stellar disk which decreases the observed velocity dispersion. Outside of the disk, the bulge dominates and the observed velocity dispersion is again higher. It should be noted that the view of the galaxy at a high inclination is crucial for this effect to be seen.

NGC4473 was discussed in the previous section where we stated that it actually contains two sub-components. One of them is flat and counter-rotates with respect to the main galaxy body. This can explain the rise of the velocity dispersion along the major axis, specifically at larger radii where the contribution of the flat component becomes similar to the main body. This is also visible in
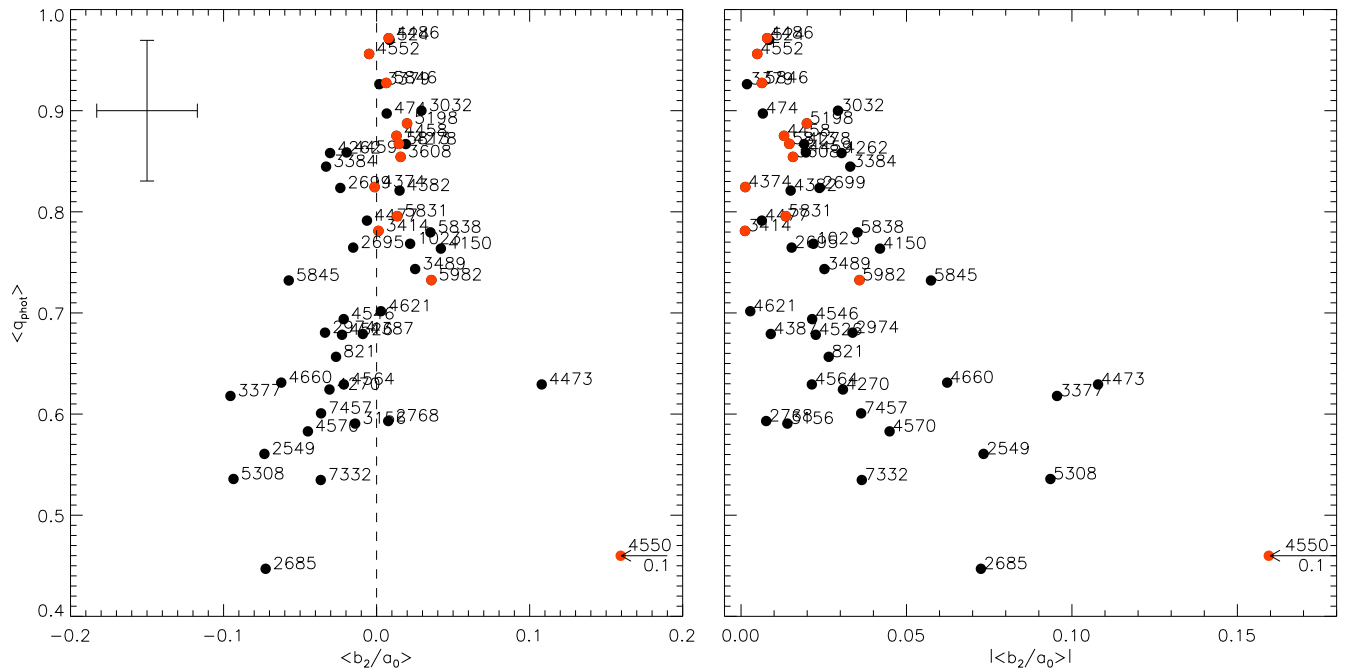
Figure 5. Left: Relation between isophotal axial ratio and the luminosity weighted average normalised second term ($\langle b_2/a_0\rangle_\sigma$) of the Fourier decomposition of the velocity dispersion profiles extracted along the isophotes. Red symbols are slow rotators. An average uncertainty, describing the radial variation of b_2/a_0 profiles, is shown in the upper left corner. Large negative $\langle b_2/a_0\rangle_\sigma$ values are typical for iso-σ contours that are rounder than the isophotes, while large positive $\langle b_2/a_0\rangle_\sigma$ values are typical for flatter iso-σ contours than the isophotes. **Right:** same as left, but now absolute values of $\langle b_2/a_0\rangle_\sigma$ are plotted. In both images, NGC4550 was shifted to the left for 0.1 for presentation purposes, as shown by the arrows.

the mean velocity map, where beyond $10''$ the velocity starts dropping. The only significant difference between these two examples is in the sense of rotation of the flat sub-components. Co-rotating disks or flattened components, viewed at favourable angles will likely show negative $\langle b_2/a_0\rangle_\sigma$, while counter-rotating components will contribute to positive $\langle b_2/a_0\rangle_\sigma$. In other words, co-rotation increases, while counter-rotation decreases the flattening of the iso-σ contours.

A similar case is NGC4550, the most extreme outlier, which also has two counter-rotating disks. NGC4150 and NGC3032 can be put in the same group: the OASIS measurements resolve their CRC components. It is interesting to note that the strongest σ-drop galaxies (NGC2768 and NGC4382) are both found on the positive side of the left hand panel of Fig. 5, admittedly with small $\langle b_2/a_0\rangle_\sigma$ (< 0.02), indicating that the shapes of the velocity dispersion maps of σ-drop objects are somewhat different from the shapes of galaxies with central plateaus in velocity dispersion profiles or bow-tie shape of velocity dispersion maps. The shapes of σ-drops are more similar to the isophotes than the shape of iso-σ contours in the objects with strong near-to edge-on disks such as NGC2549 or NGC3377. If σ-drops, bow-ties and central plateaus are all caused by disks, than the difference between them might originate from the orientation of the galaxy, where bow-ties are seen at edge-on and σ-drops at face on orientations.

Given the uncertainties, it is hard to argue either way about other galaxies with slightly positive $\langle b_2/a_0\rangle_\sigma$ values. Other effects, such as the actual size of the components or the presence of dust, may play a role on that level. This should be noted, but we, however, continue by suggesting that the main contributor to the shape difference between the zeroth and the second moment of the LOSVD in early-type galaxies are the embedded disks or flattened fast rotating components seen at different inclination. In this respect, on the right

hand panel of Fig. 5 we plot the absolute value of $\langle b_2/a_0\rangle_\sigma$. Here a trend is clear: from round slow rotators with generally small absolute values to flat fast rotating galaxies with increasing $|\langle b_2/a_0\rangle_\sigma|$. This sequence is the one of increasing contribution of the ordered rotation towards the total energy budget, but it is, unfortunately, dependent on the viewing angles (NGC524 with the face-on disk in the top left corner of the diagram) and on the luminosity-weighted contribution of the flat component to the total kinematics (CRC in NGC4621 is not detected).

4.5 Higher order moments of the LOSVD

The final part of our analysis of the kinematic moments of the LOSVD is devoted to maps of h_3 and h_4, the Gauss-Hermite moments which measure deviations of the LOSVD from a pure Gaussian. They were introduced because LOSVD profiles are rather non-Gaussian, specifically the contribution of h_3, the skewness, along the major-axis of galaxies was found to have large amplitudes (e.g. van der Marel et al. 1994). In a diagram of local $h_3 - V/\sigma$ relation, Bender et al. (1994) plotted the major axis points of their objects which could be separated in two distinct groups made of galaxies with disky isophotes and non-disky isophotes. Both groups showed anti-correlation between h_3 and V/σ, where the points with small V/σ values in the centre of the diagram had a steeper slope. It was recognised that the disky early-type galaxies cover a large range in V/σ and are responsible for tails in upper left and lower right corner of the diagram, while non-disky early-types with small V/σ values showed a somewhat smaller range in h_3 values.

On the top panel of Fig. 6 we plot the local $h_3 - V/\sigma$ relation for all data points of 48 SAURON galaxies. Red points belong to Voronoi bins of the slow rotators. This plot is somewhat differ-
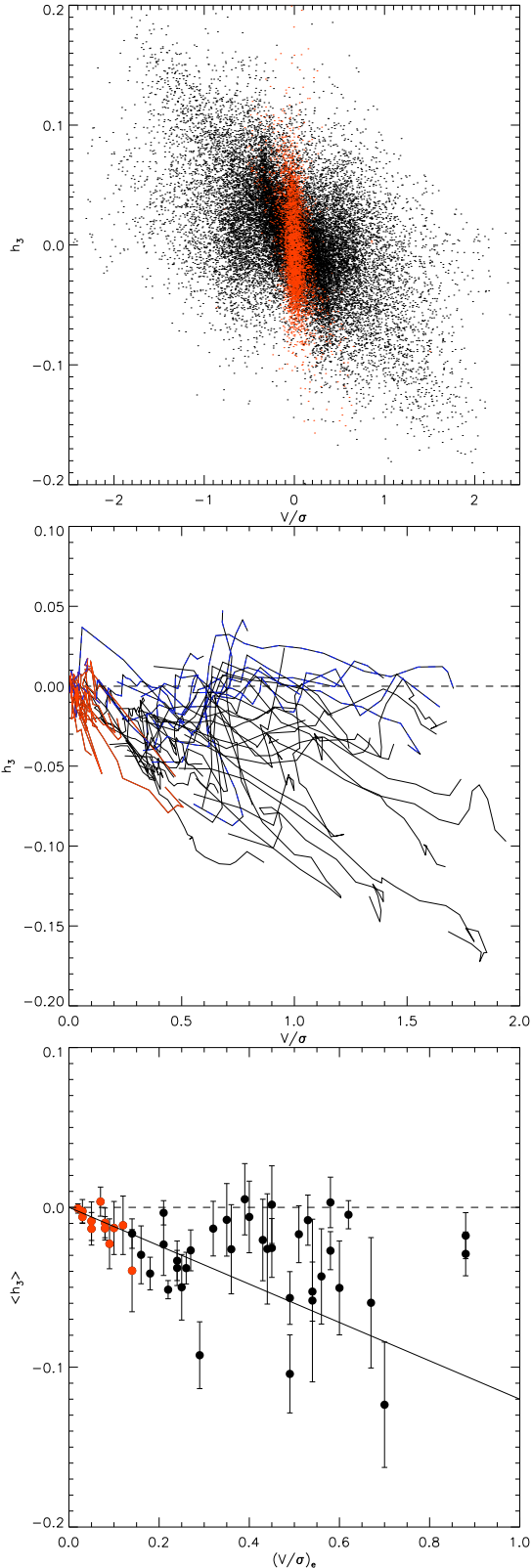
Figure 6. Top: Local $h_3 - V/\sigma$ relation for all data points of the 48 SAURON galaxies with h_3 error less than 0.2. **Middle:** Profiles of $h_3 - V/\sigma$ relation averaged on ellipses. On all maps (V, σ and h_3) profiles were extracted along the best fitting ellipses to the velocity maps. Typical error bars are of the order of 0.01 or smaller, due to averaging along the best fitting ellipse. **Bottom:** Relation between the luminosity averaged h_3 and $(V/\sigma)_e$ (V/σ within $1\,R_e$ from Paper X). The error bars describe the radial variation of h_3 profiles. The solid line is the relation from Bender et al. (1994). On all panels, slow rotators are shown in red.

ent from previous findings. Paper X showed that slow rotators have small global V/σ and this is also reflected in bin by bin values. The black points represent the Voronoi bins of fast rotators, and their distribution is different from what was found before for disky ellipticals. The shape of the distribution of black points can be described as a superposition of two components: one which is anti-correlated with V/σ and makes distinct tails in upper left and lower right corner of the diagram (large positive and negative V/σ values), and the other that is both consistent with $h_3 \sim 0$, and shows positive correlation at intermediate V/σ.

Existence of $h_3 \sim 0$ distribution of points could be explained by the fact that, while Bender et al. (1994) plot only the points along the major axis, we plot them all, and the horizontal distribution and correlating tails are the consequence of the minor axis contamination. Using kinematry we extracted profiles of the dominant harmonic terms from V, σ, and h_3 maps along the same best-fitting ellipses to the velocity maps[3]. We plot the $h_3 - V/\sigma$ profiles on the middle panel of Fig. 6. These profiles are basically major-axis representation of two-dimensional maps and are more comparable with previous major axis data. The slow rotators (in red) have the smallest V/σ values and generally small amplitudes of h_3. The two trends for fast rotators from the left-hand panel are still visible. Fast rotators cover a range of V/σ values, but some have large and some small h_3 amplitudes for a large V/σ values. In some specific cases there is a suggestion that h_3 changes the sign becoming positive and correlating with V/σ (e.g. NGC5308) at larger radii.

A confirmation of this can also be seen on the bottom panel of Fig. 6. Here we plot the relation between luminosity averaged h_3 and $(V/\sigma)_e$ obtained within $1R_e$, as advocated by Binney (2005, values taken from Paper X). The shown error bars are not statitcial uncertainties but describe the radial variation of h_3 profiles. This plot can be compared to Fig.14b of Bender et al. (1994), which also shows galaxies with $\langle h_3 \rangle \sim 0$ for intermediate V/σ_m, while their empirical fitting relation (the solid line) describes the general trend in our data.

The last kinematic moment to be analysed is given by the h_4 Gauss-Hermite coefficient. This moment describes the symmetric departures of the LOSVD from a Gaussian. It should be, however, kept in mind that it is very difficult to measure h_4 robustly, since it strongly depends on the effect of template mismatch. Also an inaccurate removal of the continuum will cause spurious h_4 values.

On the left hand panel of Fig. 7 we plot the local $h_4 - V/\sigma$ relation. Slow rotators with small V/σ values, dominate the central region. They cover a range of positive h_4 values and somewhat extend below zero. Fast rotators fill in a cloud around slow rotators, equally filling negative and positive V/σ part of the plot. There is a suggestion for a larger spread in V/σ for positive h_4 values. Luminosity weighted average $\langle h_4 \rangle$ values extracted with kinematry along the isophotes are presented as a function of luminosity-weighted V/σ measured within $1\,R_e$ (Paper X) in right panel of Fig. 7. As $(V/\sigma)_e$ increases, there is a marginal trend of an increased spread in the observed h_4 values, and galaxies with negative average values start to appear. This result is similar to Bender et al. (1994), in the sense that negative $\langle h_4 \rangle$ appear for larger $(V/\sigma)_e$, but we do not find as negative values of $\langle h_4 \rangle$. The only slow rotator with negative

---

[3] Note that here we re-run kinematry on σ maps along the best fitting ellipses for velocity maps, except in the case of the slow rotators when we used circles as explained in Section 3.2. These profiles are somewhat different from the profiles presented in Section 4.4 which were obtained along the isophotes.
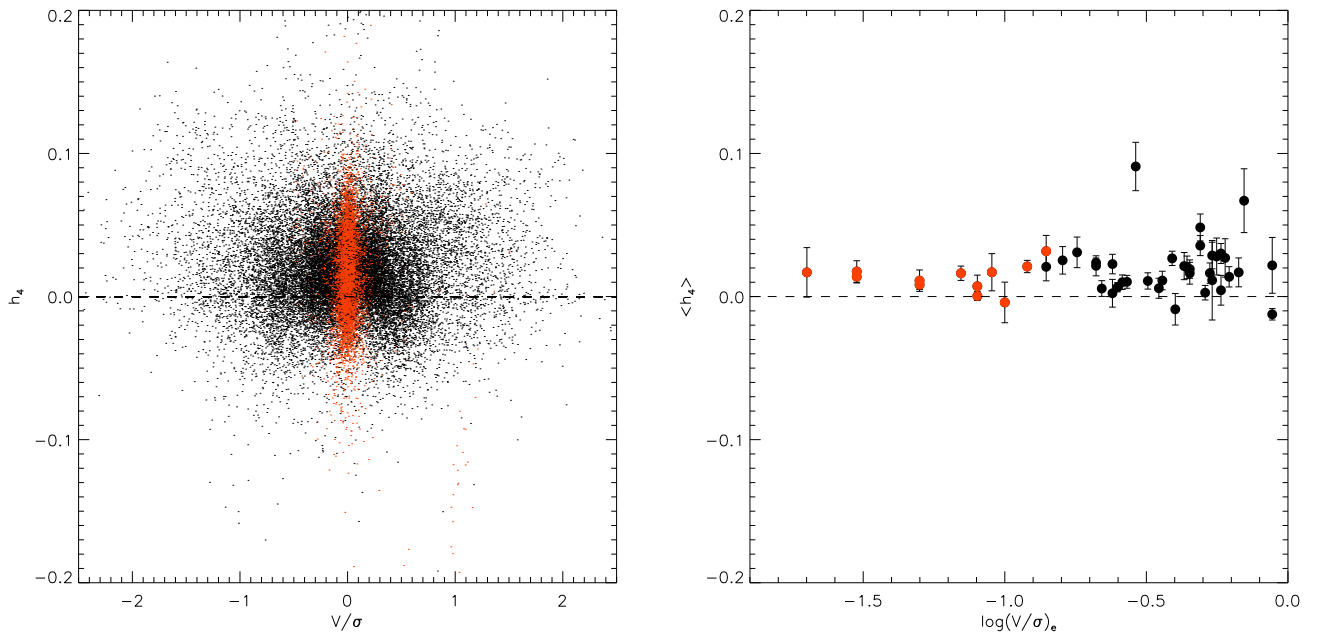
Figure 7. Right: Local correlation between h_4 and V/σ for all data points of the 48 SAURON galaxies with h_4 error less than 0.2. **Right:** Correlation between luminosity weighted values average $\langle h_4 \rangle$ and $(V/\sigma)_e$ (Paper X). Red symbols are slow rotators in both panels. The error bars describe the radial variation of h_4 profiles.

$\langle h_4 \rangle$, however, is the usual outlier, NGC4550, the special case of two counter-rotating disks.

5   DISCUSSION

5.1   Velocity maps of slow and fast rotators

Radial profiles of kinematic coefficients show that early-type galaxies are *(i)* multicomponent systems and *(ii)* in the majority of the cases contain a kinematic equivalent of a disk-like component. These statements are based on the empirical verification that the assumption of kinemetry holds. The assumption is that the azimuthal profiles, extracted from a velocity map along the best fitting ellipses, can be described with a simple cosine variation. Practically, this means that higher-order harmonic terms are negligible and at our resolution we find that the deviation from the pure cosine law is less than 2%, for about 80% of cases, at least on a part of the map. The multiple components are visible in the abrupt and localised changes of kinematic coefficients. The central regions often harbour separate kinematic components which co- or counter-rotate with respect to the outer body. In some cases there are more than two components (e.g. NGC4382) or components are similar in size and co-spatial (e.g. NGC4473). Although the axial ratio profile in edge-on systems can change with the seeing effects (see Appendix A), and in some cases the seeing can alter the map considerably, the kinematic sub-components are usually robust features.

There are, however, early-type galaxies for which the deviations from the cosine law exceed 10% across a significant radial range. Such objects are all classified as slow rotators in Paper IX. The breakdown of the kinemetry assumptions is another evidence that these objects are intrinsically different. Certainly, we might not be able to apply kinemetry *a priori* in its odd version on velocity maps that do not show odd parity (e.g. NGC4486), but in the

case of slow rotators that show a detectable level of rotation (e.g. NGC5982), the kinematic analysis clearly shows differences from the maps of fast rotators (e.g. NGC4387).

There are three types of intrinsic structures that will show small mean velocities: *(i)* face-on disks, *(ii)* two counter-rotating equal in mass and co-spatial components and *(iii)* triaxial structures. *(i) Face-on Disks.* Low inclination thin disks will still have minimal deviations from the cosine law assumed in kinemetry. Although the amplitude of the rotation in such cases is small, the disk-like rotation (negligible k_5/k_1 coefficients) is expected at all projections except in the actual case of $i = 0°$ with no rotation. Such an example in the sample is NGC524 ($i \sim 19°$). Based only on the velocity map, one could naively interpret that NGC4486 is a thin disk at $i = 0°$, given that it has $q_{kin} \sim 1$ and shows no rotation. However, other moments of the LOSVD strongly rule out this geometry, while, in general, other slow-rotators are not round enough to even be considered as such extreme cases.

(ii) Counter-rotating components. This case can be outlined with NGC4550 and NGC4473. These galaxies are examples of axisymmetric objects with two counter-rotating and co-spatial components. The first one is classified as a slow rotator, while the other one is a fast rotator. In both cases, however, it is the mass fraction of the components that really decides what is observed. In the case of NGC4550 the masses are nearly equal and the luminosity weighted mean velocity is almost zero in the central region. NGC4550 is a product of a very specific formation process, but a clear example of how a superposition of two fast rotating components can imitate a slow rotator. In NGC4473, on the other hand, one component is more massive and dominates the light in the central $10''$, where the rotation is clearly disk like. Outside this region, where the counter-rotating component starts to significantly contribute to the total light, the shape of the velocity map changes, the amplitude of the rotation drops and non-zero k_5/k_1 coefficients are necessary to describe stellar motions.
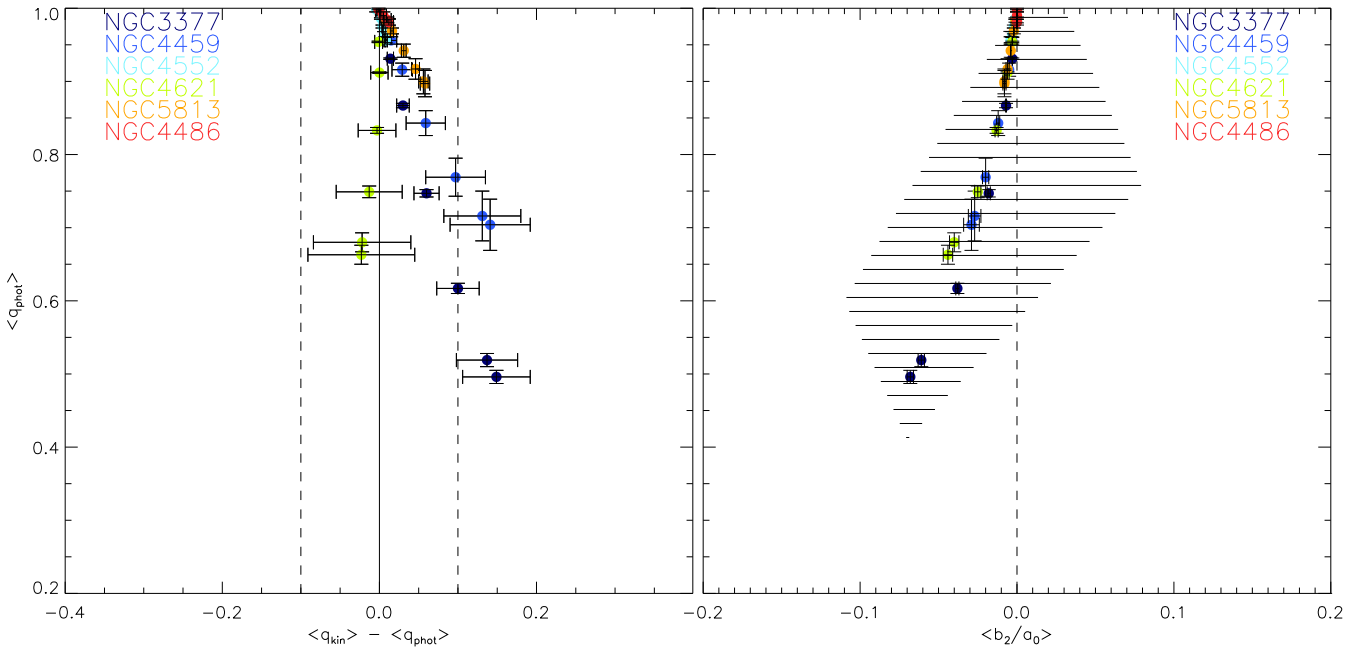
Figure 8. Left: Difference between luminosity weighted kinematic and photometric axial ratio, $\langle q_{kin} \rangle$ and $\langle q_{phot} \rangle$, for 5 Jeans models at $25°$, $35°$, $50°$, $65°$, $80°$ and $90°$ inclinations plotted against the luminosity weighted photometric axial ratio. The increase in inclination decreases $\langle q_{phot} \rangle$ and moves points downwards. The vertical dashed lines are guidelines of the variation of q_{kin} profiles from the SAURON data as in Fig. 4. Vertical solid line shows the location of zero difference between $\langle q_{phot} \rangle$ and $\langle q_{kin} \rangle$. **Right:** Relation between photometric axial ratio and absolute $\langle b_2/a_0 \rangle_\sigma$ for the same Jeans models as on the left. With increasing inclination the points move towards more negative $\langle b_2/a_0 \rangle_\sigma$ values. The hatched area represents the location of the data from Fig. 5

(iii) Triaxial objects. Observationally, these objects are marked by kinematic twists and kinematic misalignments, which are not present in axisymmetric galaxies. A strong restriction to the shape of the velocity maps of axisymmetric galaxies is that they should not have a radial variation of PA_{kin} or a misalignment between kinematic and photometric position angles. This, however, is not the case for triaxial galaxies, where the change of position angle can be influenced by a true change of the angular momentum vector, by the orientation of the viewing angles or by the relative dominance of different orbital families (Franx et al. 1991; Statler 1991; van den Bosch et al. 2008). Paper X found that, globally, kinematic misalignments are present only in slow rotating galaxies. Locally, however, we find both kinematic misalignments and twists in some fast rotating objects as well, but they are mostly confined to central components or clearly related to bars (e.g. NGC1023) or galaxies with shells (e.g. NGC474).

We do not find strong kinematic twists typical of the extreme cases of maximum entropy models of triaxial galaxies projected at various viewing angles ((Statler 1991); see also Arnold et al. (1994)) for velocity maps of Stäckel triaxial models). Given that our sample is not representative of the luminosity function of local early-type galaxies in the sense that it contains too many massive galaxies, which are also more likely to show extreme features on the velocity maps, it is remarkable that we find that only a few velocity maps are similar to those predicted. Still, the observed velocity maps are divers (e.g. the difference between the maps of slow and fast rotators) and their complexity reflects the difference in their internal structure.

The profiles of the relative change of the kinematic position angles from the first panel of Fig. 3 suggest that fast and slow rotators have genuinely different intrinsic shapes, fast rotators being mostly axisymmetric and slow rotators weakly triaxial. This is also

reflected in k_5/k_1 ratio. We suggest that the high values of this ratio in slow rotators, which is in practice caused by the noise in non-rotating velocity maps, has its origin in the internal orbital make up of these galaxies. Weakly triaxial slow rotators contain box orbits, and competing contributions of different tube orbit families, as opposed to more axisymmetric fast rotators with short-axis tubes as the only major orbit family (de Zeeuw 1985)[4]. This suggestion is also supported by the analysis of the orbital structure of collisionless merger remnants (Jesseit et al. 2005) as well as by the kinemetric analysis of velocity maps of simulated binary disc merger remnants (Jesseit et al. 2007).

5.2 Evidence for disks in fast rotators

Kinematic sub-components with azimuthal profiles that can be fitted with a cosine law are described as having a *Disk-like rotation* (DR). This does not mean that they are actual disks. It just suggests that velocity profiles of early-type galaxies extracted along the best-fitting ellipse *resemble* the velocity maps of thin disks in circular motion. The rate of occurrence of DRs is, however, striking. There is no reason why this should be the case in early-type galaxies, which in principle as a class can have a triaxial symmetry and complex motion in different planes. As suggested above, the link between the kinemetry assumption and the structure of fast rotating galaxies has its origin in their internal structure.

The results of the dynamical models in Paper X reveal that fast rotators show evidence for a kinematically distinct flattened spheroidal component, suggesting that fast rotators are

---

[4] We should keep in mind that two short-axis tube families with opposite angular momentum in certain cases can produce axisymmetric objects which appear as slow rotators, as mentioned above in the case of NGC4550.

nearly oblate and contain flattened components. In addition to these dynamically cold components, the stellar populations of fast rotators show evidence for different chemical components. Kuntschner et al. (2006) find that all morphologically flat fast rotators have Mgb line-strength distribution flatter than the isophotes, and associate it with the rotationally supported substructure, which features a higher metallicity and/or an increased Mg/Fe ratio as compared to the galaxy as a whole.

These are some of the dynamical and chemical evidences for disk-like components in fast rotators. What is the kinemetric evidence? As mentioned above, we find that velocity maps of fast rotators are mostly described by a simple cosine law, as are velocity maps of thin disks. We also find an almost one-to-one correspondence between the projected shape of the stellar distribution and the shape of the observed kinematic structure in fast rotating galaxies. The connection between the shape and the kinematics is supported by an assumption that rotation influences the shape of the object by flattening it and, for isotropic models, the rotation speed responsible for flattening of the shape is related to the shape of the stellar distribution as $\sim \sqrt{\epsilon}$ (Binney & Tremaine 2008, Section 4.8.2). In order to investigate further the $\langle q_{phot} \rangle - \langle q_{kin} \rangle$ correlation we constructed two-integral analytic models of early-type galaxies.

The isotropic models we used were previously presented in Appendix B of Paper X, to which we refer the reader for more details. The main point of these Jeans models is that we used as templates 6 galaxies, which represent some of the typical types from the SAURON sample. Their light distribution was parameterised in Paper IV by the MGE method, and was used as the basis for the intrinsic density distributions. Observables of each Jeans model were projected at 6 different inclinations: $90°$, $80°$, $65°$, $50°$, $35°$ and $25°$. These models are not meant to reproduce the observed kinematics in detail, but they are self-consistent, and under the assumption of axisymmetry and isotropy, they predict velocity maps and offer an opportunity to study the relation between the shape and kinematics.

On the left hand panel of Fig. 8 we show the difference between the luminosity-weighted average values of $\langle q_{kin} \rangle$ and $\langle q_{phot} \rangle$, measured by kinemetry on the model images and velocity maps, in the same way as for the SAURON data in Fig. 4 (also excluding the inner $5''$). Different colours represent Jeans models based on different template galaxies. Each symbol corresponds to a model at different inclination, where the points move from top to bottom with increasing inclination (from $25 - 90°$). It is clear that for small inclination $\langle q_{kin} \rangle \approx \langle q_{phot} \rangle$, but as the models are viewed closer to edge-on there is a trend of increasing differences between the axial ratios and in some cases a trend of larger variation along the profiles represented by larger error bars for progressively more inclined models. Specifically, in all but one marginal case $\langle q_{kin} \rangle > \langle q_{phot} \rangle$: in these models velocity maps are 'rounder' than images. The velocity map of the Jeans model of NGC4621, whose MGE parametrisation has the flattest Gaussian, has a flat component along the major axis, which becomes more prominent with increasing inclination, contributing to the radial variation and increasing q_{kin} with respect to q_{phot}. The kinematics of this component is the most 'disk-like' in our Jeans models with tightly pinched iso-velocity contours. For comparison, the model for NGC3377 also has a similar thin MGE component. This component contributes to the disk-like kinematic component confined to the central region, but since it is not as prominent in the total light, such as the one in the NGC4621 MGE model, only traces of the disk-like component can be seen in both photometry and kinematics.

The contrast between observed galaxies and isotropic models

is significant. The isotropic models predict $\langle q_{kin} \rangle \geq \langle q_{phot} \rangle$ for $i \gtrsim 30°$, but the models also show that prominent disk-like photometric features will generate pinched iso-velocity contours and decrease $\langle q_{kin} \rangle$ pushing the galaxies towards the observed trend of, on average, $\langle q_{kin} \rangle \sim \langle q_{phot} \rangle$ or even $\langle q_{kin} \rangle < \langle q_{phot} \rangle$. It seems reasonable to assume that while isotropic models can explain certain features of fast rotators, they cannot describe them as a class of galaxies. It is the embedded flattened components, often visible only in the kinematics that are responsible for the observed differences between the models and the data.

This can be also seen by comparing the difference in shape between the isophotes and iso-σ contours (Fig. 5). We repeated the same exercise with velocity dispersion maps of our isotropic Jeans models. Result are shown on the right panel of Fig. 8. The trend shown here of a larger absolute $\langle b_2/a_0 \rangle_\sigma$ values with lower $\langle q_{phot} \rangle$ is very similar to the observed trend (hatched region). The test can also explain the shape of the observed trend: large absolute values of $\langle b_2/a_0 \rangle_\sigma$ can be observed when the object contains a significant flattened component and it is observed at larger inclinations. The most affected are again NGC4621 and NGC3377 models. As before, the isotropic models are able to explain part of the observed data, but not the details of the distribution. Specifically, the shape of the iso-σ contours of slow rotators ($\langle b_2/a_0 \rangle_\sigma > 0$) is not reproduced well by the isotropic models. Similarly, the spread in $\langle b_2/a_0 \rangle_\sigma$ of fast rotators is also not well reproduced. Clearly, our Jeans models are much simpler than the real galaxies, lacking by construction multiple kinematic and especially counter-rotating components. Comparing the kinemetric analysis of the Jeans models and the observed objects, we find that fast rotating galaxies are more complex than isotropic rotators, presumably containing also flattened kinematically distinct components, which can co- or counter-rotate on top of the non-rotating or isotropically rotating spheroid.

The evidence for disks in fast rotators are also present in the ratio of h_3 and V/σ. h_3 measures the asymmetric deviations from the Gaussian LOSVD and the anti-correlation of h_3 with V/σ is taken to show presence of disks. Our results confirm previous findings that early-type galaxies on the whole have asymmetric LOSVDs, but this applies only to fast rotators. We also find that many fast rotators show constant and close to zero h_3 profiles, or, in a few cases, show a change from negative to positive values with increasing radius, similar to what is seen in peanut bulges and bars (Chung & Bureau 2004; Bureau & Athanassoula 2005)

The embedded flattened components in fast rotators are also evident when $h_3 - V/\sigma$ diagram is compared with the results of merger simulations (Balcells 1991; Bendo & Barnes 2000; Naab & Burkert 2001; González-García et al. 2006). Specifically, the updated $h_3 - V/\sigma$ diagram in Fig. 6 can be compared with Fig.16 from Naab et al. (2006), who discuss the influence of dissipational mergers in which embedded disks are formed in merger remnants. Our figure compares rather well with a combination of 1:1 dry and 1:3 wet mergers. This comparison suggest that it is not possible to explain the LOSVD of early-type galaxies with one merging track only, but that slow rotators predominantly originate in major colissionless mergers, while fast rotators are remnants of dissipational mergers.

The comparison of our bin-by-bin $h_4 - V/\sigma$ diagram (right-hand panel in Fig. 7) and lower four panels of Fig.16 in Naab et al. (2006) is equally impressive, although their simulations predict somewhat too negative values of h_4. Again, the observations are largely consistent with the scenario where slow rotators originate

from dry 1:1 mergers, while fast rotators from a combination of dry and wet 1:3 mergers.

Combining all the evidence presented in the previous section, we suggest that fast rotators are dominated by disks (e.g. NGC3156, NGC2685). When their light is dominated by the bulge, their kinematics still show strong disk components (e.g. NGC821, NGC4660). In either case, *fast rotators contain flattened fast rotating components and this dynamical property differentiates them from slow rotators*. We suggest that with increasing specific angular momentum, λ_R, the relative mass of the embedded disks also increases and contributes more significantly to the total mass. Among the disk-like components in fast rotators there is a range of flattenings reflecting a diversity in possible formation paths which create, preserve and/or thicken disks within spheroids, such as passive fading of spirals and multiple minor dissipational mergers. The change within the internal structure is observationally reflected in the transition between slow and fast rotators, which offers possible anchor points for theoretical models of galaxy evolution.

6 CONCLUSIONS

Using kinemetry we analysed two-dimensional maps of 48 early-type galaxies observed with SAURON and velocity maps of a sub-sample observed with OASIS. The analysed maps are: reconstructed image, mean velocity, velocity dispersion, h_3 and h_4 Gauss-Hermite moments. The reconstructed images and the maps of the mean velocity were analysed along the best fit ellipses. Maps of the higher moments of the LOSVD were analysed either along the isophotes (velocity dispersion, h_4) or best-fitting ellipses from velocity maps (h_3). We presented the profiles of kinemetric coefficients for velocity maps, being the dominant kinematic moment of the LOSVD and having the highest signal-to-nose ratio.

Kinemetry and its kinemetric coefficients allow us *(i)* to differentiate between slow and fast rotators from velocity maps only and *(ii)* to indicate that fast rotating galaxies contain disks with a larger range in the mass fractions to the main body. The results of this work can be summarised as follows:

• Following the kinemetric analysis of the velocity maps it is possible to distinguish between galaxies with *Single* and *Multiple Components*. Components can be described as having a *Disk-like rotation*, *Low-level velocity*, *Kinematic misalignment*, *Kinematic twist* or being *Kinematically Decoupled Component*. The sorting of galaxies in these groups is based on kinemetric coefficients: PA_{kin}, q_{kin}, k_1 and k_5/k_1.

• The majority of early-type galaxies are MC systems (69%)

• The total fraction of galaxies with a DR component (including all that have $k_5/k_1 < 0.02$) is 81%. In terms of S0/E classification, 92% of S0s and 74% of Es have components with disk-like kinematics.

• KDCs are found in 29% of galaxies. These KDC are of different sizes, some are not resolved at SAURON resolution and appear as CLVs, but are clearly detectable in the OASIS observations at higher spatial resolution.

• Early-type galaxies with constant $PA_{kin}(\Delta PA < 10°$ outside any central component) are fast rotators. All fast-rotators have a DR component.

• Most fast rotators have $\langle q_{kin} \rangle \lesssim \langle q_{phot} \rangle$. Their kinematics often show a structure flatter than the distribution of light. This means that images alone are not sufficient to recognise all fast rotators (e.g. NGC524 or N3379 would be missed)

• In face-on galaxies, isophotes are coincident with iso-σ contours. In edge-on galaxies, however, there are differences which can be detected with kinemetry. Specifically, the edge-on fast rotators contain dynamically cold components which changes the shape of iso-σ contours.

• Slow rotating galaxies have low V/σ and a range in h_3 amplitudes. Fast rotating galaxies have large spread in h_3 which anti-correlates with V/σ. There is, however, a significant number of fast rotating galaxies which have h_3 radial profiles that change from strongly negative to near to zero h_3 values. Similar behaviour was found in bar galaxies or in remnants of colissionless mergers.

• Allowing for large uncertainties in the determination of h_4, our data show a trend where slow and fast rotators have similar h_4 values, with a weak tendency for an increased spread of h_4 in fast rotators, also dependant on V/σ. These trends can be explained through a combination of dry and wet mergers of both equal and unequal in mass progenitors.

• Dissimilarities between slow and fast rotators originate in their different internal structures. Slow rotators are mildly triaxial objects supporting a variety of orbital families. Fast rotators are axisymmetric spheroids with embedded flattened components of different mass fraction ranging from completely disk dominated systems to small central disks visible only in kinematics.

REFERENCES

Arnold R., de Zeeuw P. T., Hunter C., 1994, MNRAS, 271, 924

Bacon R., Adam G., Baranne A., Courtes G., Dubet D., Dubois J. P., Emsellem E., Ferruit P., Georgelin Y., Monnet G., Pecontal E., Rousset A., Say F., 1995, A&AS, 113, 347

Bacon R., Copin Y., Monnet G., Miller B. W., Allington-Smith J. R., Bureau M., Carollo C. M., Davies R. L., Emsellem E., Kuntschner H., Peletier R. F., Verolme E. K., de Zeeuw P. T., 2001, MNRAS, 326, 23

Balcells M., 1991, A&A, 249, L9

Bender R., 1988a, A&A, 202, L5

Bender R., 1988b, A&A, 193, L7

Bender R., Doebereiner S., Moellenhoff C., 1988, A&AS, 74, 385

Bender R., Saglia R. P., Gerhard O. E., 1994, MNRAS, 269, 785

Bender R., Surma P., Doebereiner S., Moellenhoff C., Madejsky R., 1989, A&A, 217, 35

Bendo G. J., Barnes J. E., 2000, MNRAS, 316, 315

Bertola F., Capaccioli M., 1975, ApJ, 200, 439

Binney J., 1978, MNRAS, 183, 501

Binney J., 1980, MNRAS, 190, 873

Binney J., 2005, MNRAS, 363, 937

Binney J., Tremaine S., 2008, Galactic dynamics. Princeton, NJ, Princeton University Press, 2008, second edition

Bureau M., Athanassoula E., 2005, ApJ, 626, 159

Cappellari M., 2002, MNRAS, 333, 400

Cappellari M., Bacon R., Bureau M., Damen M. C., Davies R. L., de Zeeuw P. T., Emsellem E., Falcón-Barroso J., Krajnović D., Kuntschner H., McDermid R. M., Peletier R. F., Sarzi M., van den Bosch R. C. E., van de Ven G., 2006, MNRAS, 366, 1126

Cappellari M., Copin Y., 2003, MNRAS, 342, 345

Cappellari M., Emsellem E., Bacon R., Bureau M., Davies R. L., de Zeeuw P. T., Falcón-Barroso J., Krajnović D., Kuntschner H., McDermid R. M., Peletier R. F., Sarzi M., van den Bosch R. C. E., van de Ven G., 2007, MNRAS, 379, 418

Chung A., Bureau M., 2004, AJ, 127, 3192

Ciotti L., Lanzoni B., 1997, A&A, 321, 724

Corsini E. M., Wegner G., Saglia R. P., Thomas J., Bender R., Thomas D., 2008, ApJS, 175, 462

Davies R. L., Efstathiou G., Fall S. M., Illingworth G., Schechter P. L., 1983, ApJ, 266, 41

de Zeeuw P. T., 1985, MNRAS, 216, 273

de Zeeuw P. T., Bureau M., Emsellem E., Bacon R., Carollo C. M., Copin Y., Davies R. L., Kuntschner H., Miller B. W., Monnet G., Peletier R. F., Verolme E. K., 2002, MNRAS, 329, 513

Djorgovski S., 1983, Journal of Astrophysics and Astronomy, 4, 271

Emsellem E., Cappellari M., Krajnović D., van de Ven G., Bacon R., Bureau M., Davies R. L., de Zeeuw P. T., Falcón-Barroso J., Kuntschner H., McDermid R., Peletier R. F., Sarzi M., 2007, MNRAS, 379, 401

Emsellem E., Cappellari M., Peletier R. F., McDermid R. M., Geacon R., Bureau M., Copin Y., Davies R. L., Krajnović D., Kuntschner H., Miller B. W., de Zeeuw P. T., 2004, MNRAS, 352, 721

Emsellem E., Monnet G., Bacon R., 1994, A&A, 285, 723

Falcón-Barroso J., Bacon R., Bureau M., Cappellari M., Davies R. L., de Zeeuw P. T., Emsellem E., Fathi K., Krajnović D., Kuntschner H., McDermid R. M., Peletier R. F., Sarzi M., 2006, MNRAS, 369, 529

Franx M., Illingworth G., de Zeeuw P. T., 1991, ApJ, 383, 112

Gebhardt K., Richstone D., Tremaine S., Lauer T. R., Bender R.,

Bower G., Dressler A., Faber S. M., Filippenko A. V., Green R., Grillmair C., Ho L. C., Kormendy J., Magorrian J., Pinkney J., 2003, ApJ, 583, 92

Gerhard O., Kronawitter A., Saglia R. P., Bender R., 2001, AJ, 121, 1936

Gerhard O. E., 1993, MNRAS, 265, 213

González-García A. C., Balcells M., Olshevsky V. S., 2006, MNRAS, 372, L78

Halliday C., Davies R. L., Kuntschner H., Birkinshaw M., Bender R., Saglia R. P., Baggley G., 2001, MNRAS, 326, 473

Hau G. K. T., Forbes D. A., 2006, MNRAS, 371, 633

Hernquist L., 1990, ApJ, 356, 359

Hubble E. P., 1936, Yale University Press

Illingworth G., 1977, ApJ, 218, L43

Jedrzejewski R. I., 1987, MNRAS, 226, 747

Jesseit R., Naab T., Burkert A., 2005, MNRAS, 360, 1185

Jesseit R., Naab T., Peletier R. F., Burkert A., 2007, MNRAS, 376, 997

Koprolin W., Zeilinger W. W., 2000, A&AS, 145, 71

Kormendy J., 1982, in Martinet L., Mayor M., eds, Saas-Fee Advanced Course 12: Morphology and Dynamics of Galaxies Observations of galaxy structure and dynamics. pp 113–288

Kormendy J., Bender R., 1996, ApJ, 464, L119+

Kormendy J., Illingworth G., 1982, ApJ, 256, 460

Krajnović D., Cappellari M., de Zeeuw P. T., Copin Y., 2006, MNRAS, 366, 787

Kronawitter A., Saglia R. P., Gerhard O., Bender R., 2000, A&AS, 144, 53

Kuntschner H., Emsellem E., Bacon R., Bureau M., Cappellari M., Davies R. L., de Zeeuw P. T., Falcón-Barroso J., Krajnović D., McDermid R. M., Peletier R. F., Sarzi M., 2006, MNRAS, 369, 497

Lauer T. R., 1985, ApJS, 57, 473

McDermid R. M., Emsellem E., Shapiro K. L., Bacon R., Bureau M., Cappellari M., Davies R. L., de Zeeuw T., Falcón-Barroso J., Krajnović D., Kuntschner H., Peletier R. F., Sarzi M., 2006, MNRAS, 373, 906

Merritt D., Quinlan G. D., 1998, ApJ, 498, 625

Naab T., Burkert A., 2001, ApJ, 555, L91

Naab T., Jesseit R., Burkert A., 2006, MNRAS, 372, 839

Peletier R. F., Davies R. L., Illingworth G. D., Davis L. E., Cawson M., 1990, AJ, 100, 1091

Qian E. E., de Zeeuw P. T., van der Marel R. P., Hunter C., 1995, MNRAS, 274, 602

Rix H., White S. D. M., 1990, ApJ, 362, 52

Rix H.-W., Carollo C. M., Freeman K., 1999, ApJ, 513, L25

Rix H.-W., Franx M., Fisher D., Illingworth G., 1992, ApJ, 400, L5

Rubin V. C., Graham J. A., Kenney J. D. P., 1992, ApJ, 394, L9

Ryden B. S., Terndrup D. M., Pogge R. W., Lauer T. R., 1999, ApJ, 517, 650

Saglia R. P., Bertschinger E., Baggley G., Burstein D., Colless M., Davies R. L., McMahan Jr. R. K., Wegner G., 1997, ApJS, 109, 79

Sandage A., 1961, The Hubble atlas of galaxies. Washington: Carnegie Institution, 1961

Sandage A., Bedke J., 1994, The Carnegie atlas of galaxies. Washington, DC: Carnegie Institution of Washington with The Flintridge Foundation, —c1994

Sandage A., Sandage M., Kristian J., 1975, Galaxies and the Universe. Galaxies and the Universe

Schweizer F., 1979, ApJ, 233, 23

Schweizer F., 1981, AJ, 86, 662

Statler T. S., 1991, AJ, 102, 882

Tremaine S. D., 1987, in de Zeeuw P. T., ed., Structure and Dynamics of Elliptical Galaxies Vol. 127 of IAU Symposium, Summary - Structure and Dynamics of Elliptical Galaxies. pp 367–+

van den Bergh S., 1990, ApJ, 348, 57

van den Bosch R. C. E., van de Ven G., Verolme E. K., Cappellari M., de Zeeuw P. T., 2008, MNRAS, 385, 647

van der Kruit P. C., Allen R. J., 1978, ARA&A, 16, 103

van der Marel R. P., 1991, MNRAS, 253, 710

van der Marel R. P., 1994, MNRAS, 270, 271

van der Marel R. P., Franx M., 1993, ApJ, 407, 525

van der Marel R. P., Rix H. W., Carter D., Franx M., White S. D. M., de Zeeuw T., 1994, MNRAS, 268, 521

Wegner G., Corsini E. M., Saglia R. P., Bender R., Merkl D., Thomas D., Thomas J., Mehlert D., 2002, A&A, 395, 753

APPENDIX A: INFLUENCE OF SEEING ON THE SHAPE OF THE VELOCITY MAPS

The effects of seeing on galaxy images in the regime of non-adaptive optic assisted observations are now well understood (Saglia et al. 1997). They are specifically important in the nuclear regions where the instrumental effects and the atmospheric seeing redistribute photons sufficiently enough to change the intrinsic ellipticity or position angle and mask structures like concentrated stellar nuclei or double nuclei (Schweizer 1979, 1981; Djorgovski 1983; Lauer 1985). Specifically, luminosity profiles are affected more by the seeing when the ellipticity is low, while the ellipticity profiles are affected more when the ellipticity is high (Peletier et al. 1990). In general, effects of seeing can be detected to quite large radii.

It is natural to expect the redistribution of photons due to the seeing will also influence the two-dimensional shape (maps) of the higher moments of the LOSVD. Specifically, for the first moment, the mean velocity, the obvious effect of larger seeing is a less steep rise of the velocity in the centre. Additionally, one can expect an increased axial ratio (rounder map), or in other words, a more open spider diagram in the central regions. Except for these qualitative expectations there are no quantitative estimates of the influence of seeing on the shape of velocity maps. Observations of the SAURON sample were taken under a variety of atmospheric conditions, so before analysing the velocity maps, we tested the effects of different PSFs.

We constructed a number of model velocity maps using a Hernquist (1990) potential which reasonably well approximates the density of real early-type galaxies. Each model map was constructed from the Hernquist circular velocity profile, projected at a certain inclination to imitate different axial ratios seen in the sample (q_{kin}), and weighted by the given Hernquist surface brightness profiles. All models have the same scale length $r_0 = 10''$. The inclinations ranged from 20 to 75 degrees, where 0 and 90 degrees are face on and edge on viewing angles, respectively. This corresponds to velocity maps with axial ratios q_{kin} in the range of 0.94 to 0.26. Although in the SAURON sample there are near to edge on galaxies, their velocity maps do not resemble the limiting case of edge on disks (q_{kin}=0), being considerably less flat. The above range in axial ratios were used to match the values observed in the SAURON sample. Maps were then convolved with a Gaussian kernel of different full-width-half-maximum (FWHM), accounting also for the square pixels (Qian et al. 1995) in such a way as to make the model

maps similar to observations, especially in the central regions which remain unbinned. The range of FWHM was also matched to the measured seeing range of SAURON observations (Paper III). Figure A1 shows an example of model maps for axial ratio of 0.5 and seeing FWHMs of $1''$, $2''$ and $3''$.

We ran kinemetry on the convolved model velocity maps and extracted the same parameters as for the observed velocity maps: PA_{kin}, q_{kin}, k_1 and k_5/k_1 harmonics. The results can be seen in Fig. A2 and they suggest that:

- determination of the position angle is not influenced by the seeing;
- the influence of the seeing on the determined axial ratio is larger on maps with intrinsically smaller axial ratio. Also, the bigger the seeing is, the rounder (larger axial ratio) is the observed map.
- the influence of the seeing on the rotation curve (k_1 term) is larger on maps with intrinsically smaller axial ratios, where the bigger is the seeing, the lower is the maximum velocity. The position of maximum velocity is also pushed towards larger radii.
- the influence of the seeing on the higher terms (k_5/k_1) is negligible in most cases, except for intrinsically very flat maps, but even there the signal is of the order of 1% or less and is not detectable with the current accuracy.

As expected, the seeing influences the axial ratio of velocity maps (or, in other words, the opening of the iso-velocity contours), and the steepness of the rotation curve, both in the maximum values and the positions of these maxima.

The largest effect is for maps with small axial ratio (large opening angles), which can be understood as the consequence of the convolution, similar as in the case of photometry and high ellipticity. In terms of changing of the intrinsic values, it is the axial ratio that is the most affected by seeing. At an intrinsic flattening of 0.77, a bad seeing of $2''.5$, will increase the flattening by 0.1. This effect rises to surprising 0.5 difference in measured flattening for an intrinsic flattening of 0.26. This effect is milder for the maximum rotation velocity, where only for velocity maps with the smallest axial ratios and strongest seeings the difference between the intrinsic and seeing convolved values exceeds 10 km/s. Another effect of seeing on the velocity maps is the change of position of the maximum axial ratio and the maximum rotational velocity with increasing seeing. In both cases the trend is clear: larger seeing FWHM causes displacement of the maximum (q_{kin} or k_1) towards larger radii.

In summary, seeing can strongly influence the appearance of the velocity maps, both in the shape, value and extent of the features. This is important for interpreting the structures on the maps and, especially, when looking for kinematic subcomponents.

APPENDIX B: KINEMETRIC PROFILES

In this section we present the results of kinemetric analysis of SAURON velocity maps.
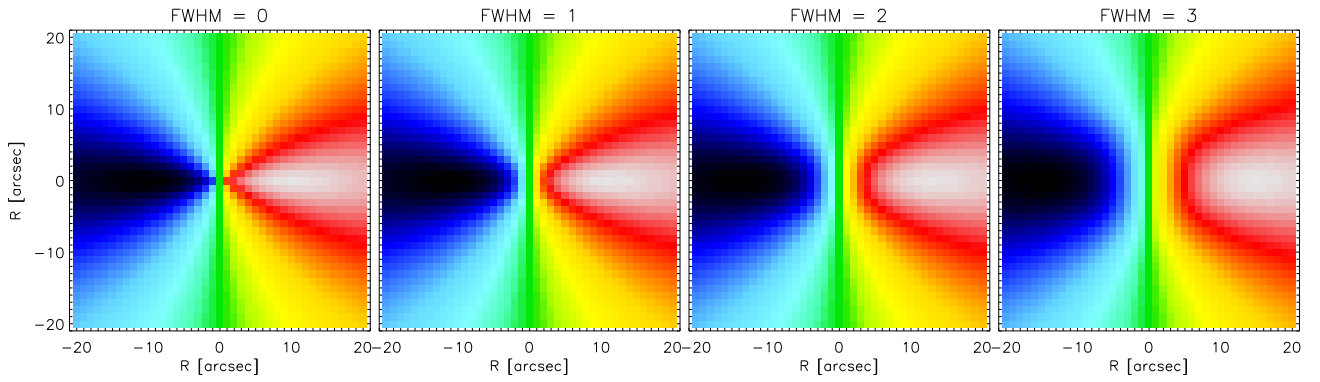
Figure A1. An example of model velocity maps for a given inclination and convolved with different seeing kernels. **From left to right:** A model velocity map at axial ratio of 0.5 prior to convolution with seeing. Model velocity maps convolved with $1''$, $2''$ and $3''$ FWHM seeing, respectively. Note the change in the iso-velocity contours in the centre with the increasing seeing.
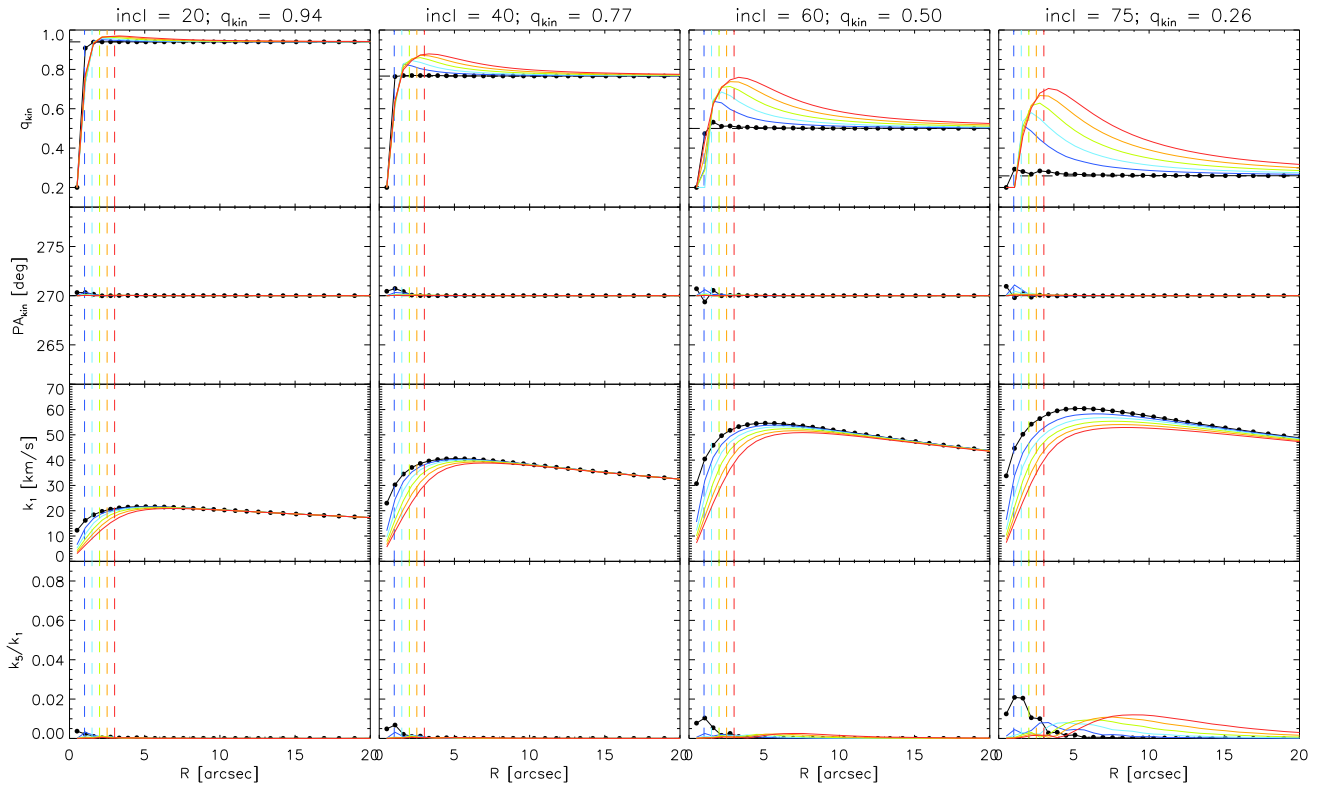
Figure A2. Kinemetric analysis of seeing convolved model velocity maps. **From left to right:** Kinemetry coefficients from maps with axial ratios of 0.94, 0.77, 0.5 and 0.26 degrees. **From top to bottom:** Kinemetric coefficients: position angle, axial ratio, k_1 and k_5/k_1 harmonics. Colours correspond to values extracted from maps convolved to different seeing. Black: unconvolved model map. Blue: model map convolved with FWHM of $1''$. Light blue: model map convolved with FWHM of $1.''5$. Green: model map convolved with FWHM of $2''$. Yellow: model map convolved with FWHM of $2.''5$. Orange: model map convolved with FWHM of $3''$. Vertical lines show the radial extent of the seeing at FWHM. Note that the incorrect determination of axial ratio at the innermost radius is an artifact of poor sampling.
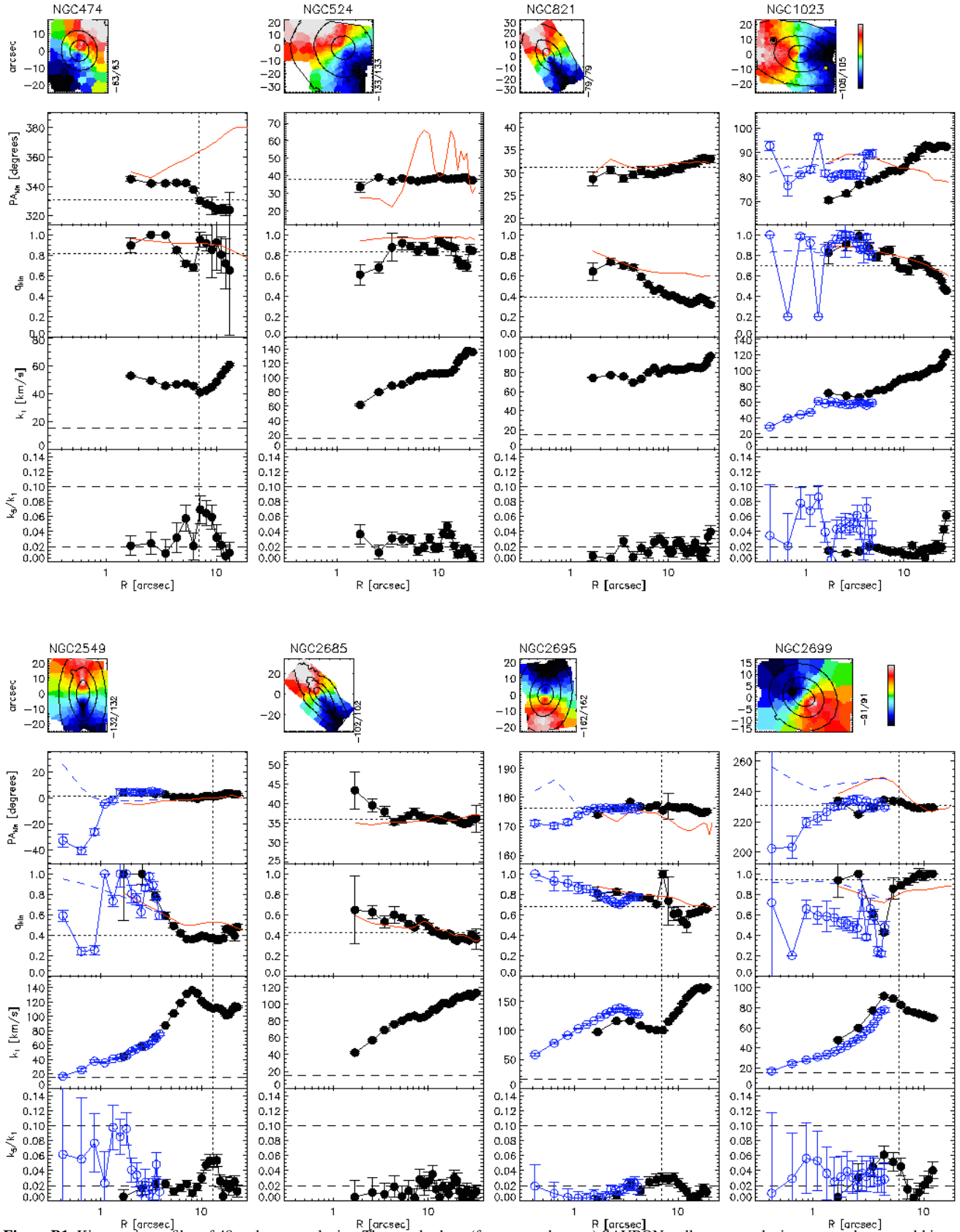
Figure B1. Kinematric profiles of 48 early-type galaxies. The panels show (from top to bottom) SAURON stellar mean velocity map, and extracted kinematric properties: position angle, axial ratio, k_1 and k_5/k_1 coefficients. Solid black symbols are SAURON data, open blue circles are OASIS data. Solid light-blue and green symbols are results of kinemetry on circles for OASIS and SAURON data, respectively. Red line shows photometric PA_{phot} and q_{phot} from the SAURON reconstructed images. Dashed-blue line shows photometric PA_{phot} and $1 - \epsilon$ from the OASIS reconstructed images. Dashed horizontal lines on k_1 and k_5/k_1 panels show the limiting cases: $k_1 = 15$ km s^{-1} limit of detectable rotation, $k_5/k_1 = 0.02$ limit of detectable deviation from the assumed cosine function in kinemetry, $k_5/k_1 = 0.1$ limit for doing kinemetry on circles. These limits are data dependant (for more details see Section 4). Dashed lines on PA_{kin} and q_{kin} panels show luminosity weighted average values of the radial profiles. In the case of global $\langle q_{kin} \rangle$ innermost 5″ are excluded due to the seeing effects.
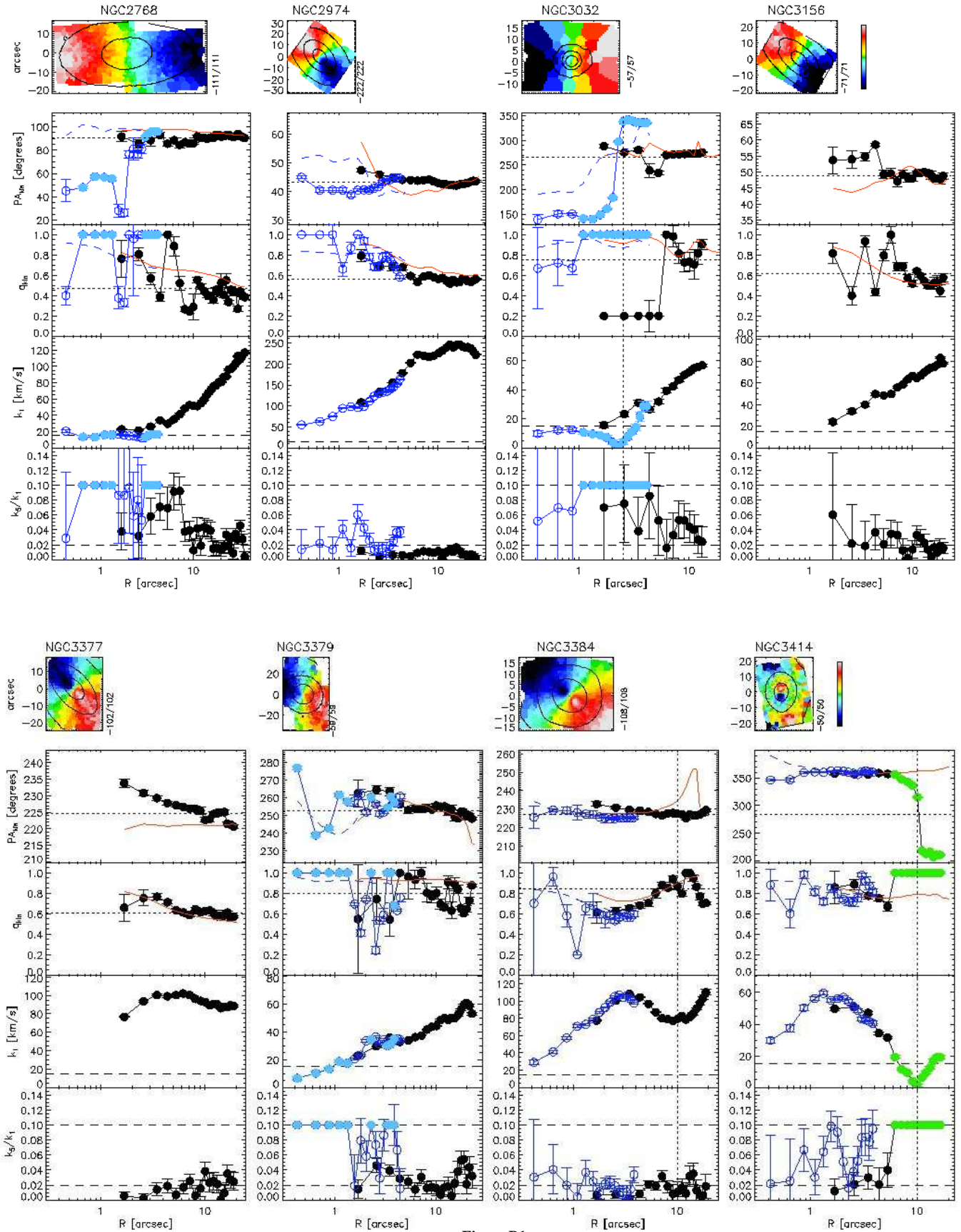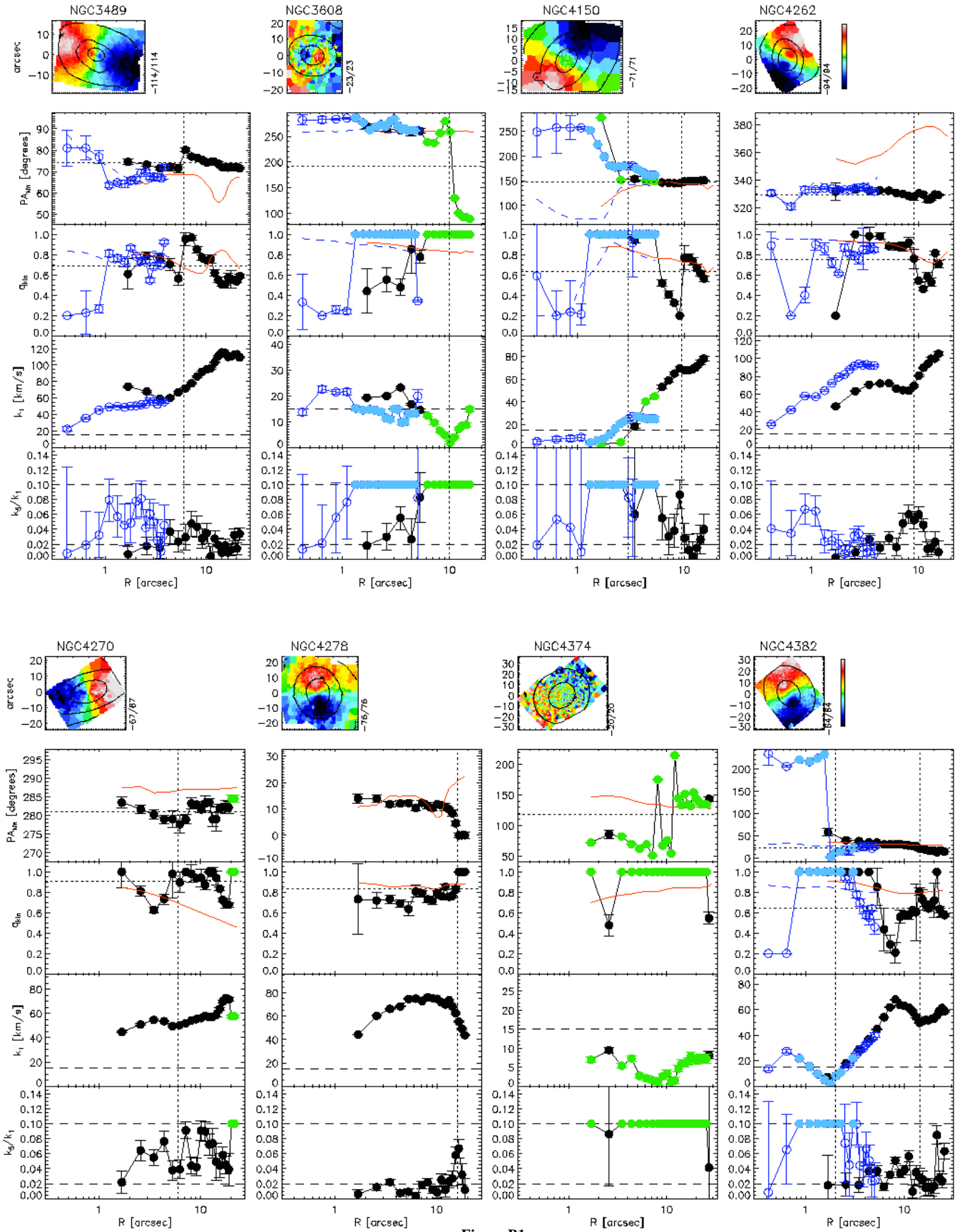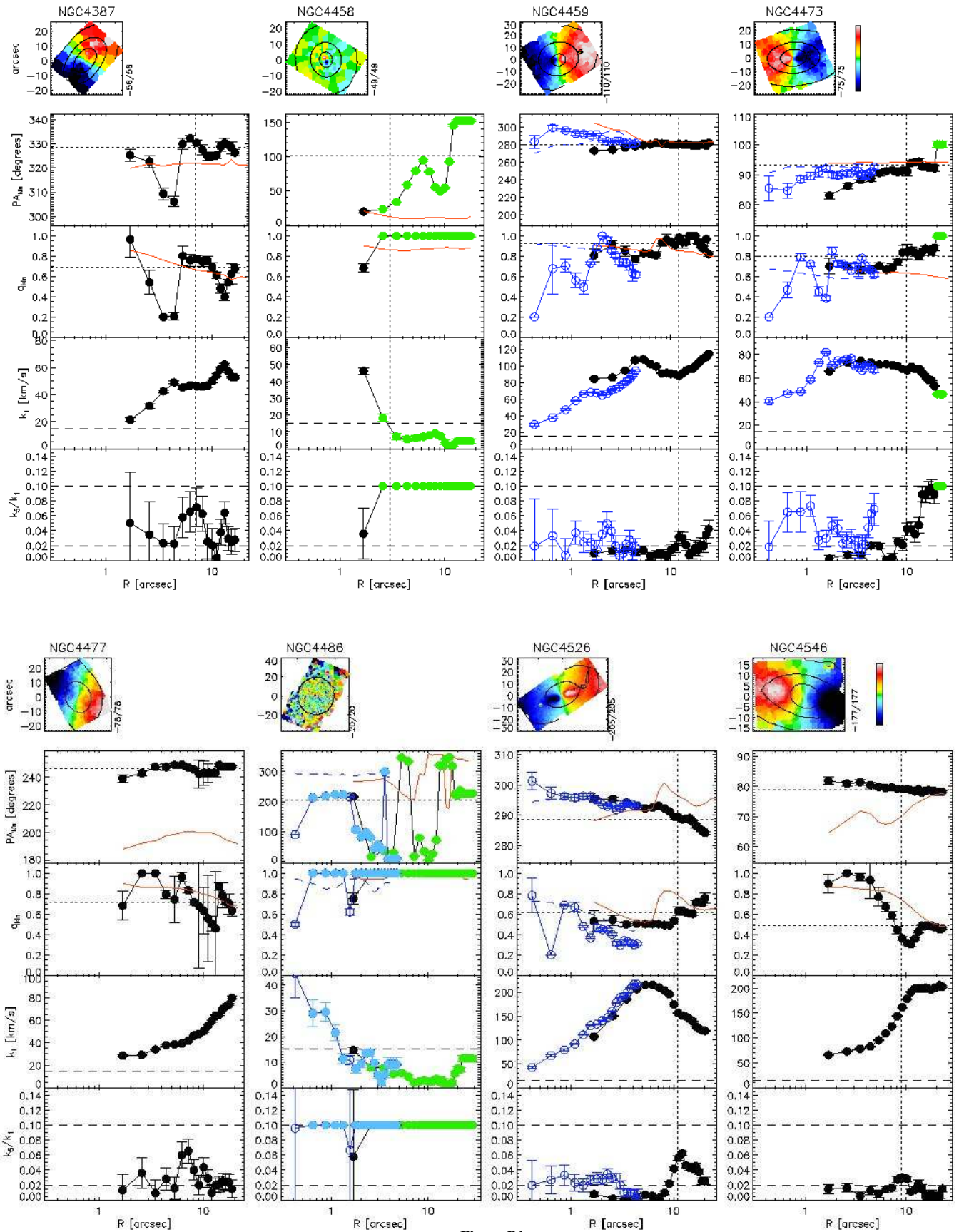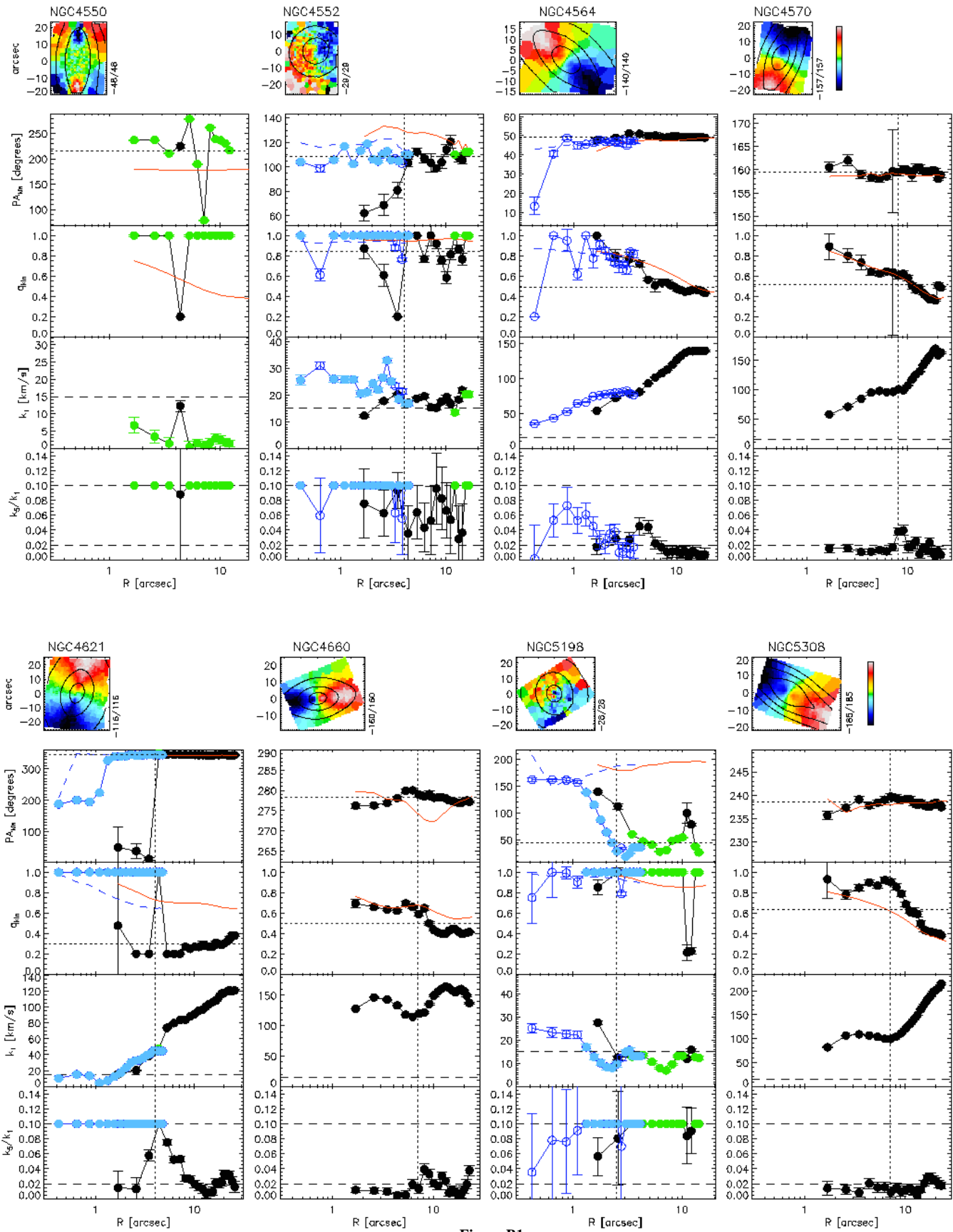
Figure B1.

Figure B1.

Figure B1.

Figure B1.

Figure B1.